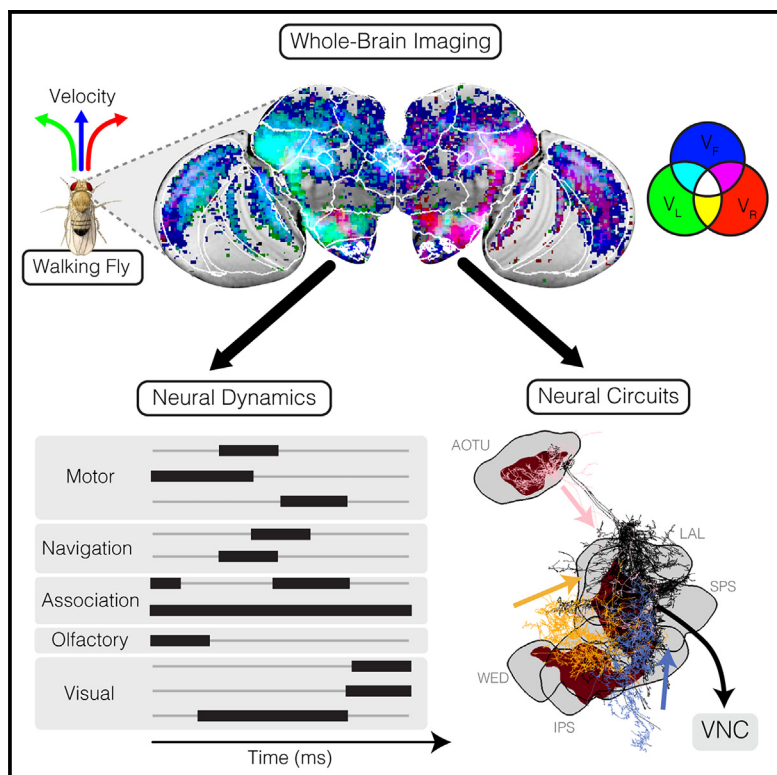


### Mapping the neural dynamics of locomotion across the *Drosophila* brain

#### Graphical abstract



#### Authors

Bella E. Brezovec, Andrew B. Berger,  
Yukun A. Hao, Feng Chen,  
Shaul Druckmann,  
Thomas R. Clandinin

Correspondence  
trc@stanford.edu

#### In brief

Brezovec et al. map the brain-wide neural dynamics associated with locomotion in *Drosophila*. Walking maneuvers coincide with waves of neural activity that sweep across the brain along stereotyped trajectories. Connectome alignment identifies candidate neural networks underlying walking behavior.

#### Highlights

- Whole-brain imaging of walking *Drosophila* reveals extensive topographic structure
- Neurons with similar tuning for forward or angular velocity are spatially clustered
- Temporal trajectories of neural activity sweep across the topographic maps
- Connectome registration identifies candidate networks underlying walking behavior



## Article

# Mapping the neural dynamics of locomotion across the *Drosophila* brain

Bella E. Brezovec,<sup>1</sup> Andrew B. Berger,<sup>1</sup> Yukun A. Hao,<sup>1</sup> Feng Chen,<sup>1</sup> Shaul Druckmann,<sup>1</sup> and Thomas R. Clandinin<sup>1,2,\*</sup>

<sup>1</sup>Department of Neurobiology, Stanford University, Fairchild D200, 299 W. Campus Drive, Stanford, CA 94305, USA

<sup>2</sup>Lead contact

\*Correspondence: trc@stanford.edu

<https://doi.org/10.1016/j.cub.2023.12.063>

## SUMMARY

Locomotion engages widely distributed networks of neurons. However, our understanding of the spatial architecture and temporal dynamics of the networks that underpin walking remains incomplete. We use volumetric two-photon imaging to map neural activity associated with walking across the entire brain of *Drosophila*. We define spatially clustered neural signals selectively associated with changes in either forward or angular velocity, demonstrating that neurons with similar behavioral selectivity are clustered. These signals reveal distinct topographic maps in diverse brain regions involved in navigation, memory, sensory processing, and motor control, as well as regions not previously linked to locomotion. We identify temporal trajectories of neural activity that sweep across these maps, including signals that anticipate future movement, representing the sequential engagement of clusters with different behavioral specificities. Finally, we register these maps to a connectome and identify neural networks that we propose underlie the observed signals, setting a foundation for subsequent circuit dissection. Overall, our work suggests a spatiotemporal framework for the emergence and execution of complex walking maneuvers and links this brain-wide neural activity to single neurons and local circuits.

## INTRODUCTION

Topographic maps have provided fundamental insights into the functional organization of the brain. Such maps of neural activity have revealed spatial order in sensory systems, motor control, and cognitive processing in many different animals.<sup>1–4</sup> The existence of these functional maps reflects the fact that neural processing is often distributed across large populations of cells whose spatial arrangements reveal coding principles of the system. For example, functional maps of motor cortex in primates have revealed how movements of different limbs are spatially segregated, a necessary step to revealing how specific movement trajectories are encoded by the dynamics of neural populations.<sup>5–8</sup> Here, we develop an imaging and analysis pipeline to describe both the precise spatial architecture of the brain-wide circuits that are engaged by walking in *Drosophila*, as well as the temporal flow of information across these maps as behavior emerges. This spatiotemporal order reveals how individual walking maneuvers sequentially engage different, widely distributed neural substructures.

We have chosen to apply our pipeline to a fundamental, flexible, and incompletely understood behavior: walking. Walking subserves a diverse array of behavioral goals in many animals and must be shaped by both sensory inputs and internal states. Despite its central role, locomotor control is incompletely understood.<sup>9–11</sup> In vertebrates, many brain regions play key roles in shaping locomotion, including the basal ganglia, brainstem, cerebellum, motor cortex, and spinal cord.<sup>12–14</sup> More recently, broad swaths of both sensory and non-sensory cortex have

been shown to contain motor-related signals.<sup>15–20</sup> In addition, brain-wide signatures of neural activity associated with swimming and crawling have been measured in larval zebrafish, larval *Drosophila*, and *C. elegans*.<sup>21–31</sup> Moreover, recent work has described whole-brain imaging techniques in adult flies in the context of state-dependent changes in activity and metabolism,<sup>32–36</sup> as well as sensory-evoked responses.<sup>37–39</sup> Given the accumulating evidence across species for widespread distribution of motor signatures, directly measuring how these signals are ordered in space and time relative to one another is likely to provide insight into how the brain produces walking behavior.

Insects have long provided valuable insights into the biomechanics and neural control of locomotion.<sup>40–44</sup> More recently, the scalability of *Drosophila* behavioral measurements has allowed a variety of quantitative descriptions of the structure of walking dynamics in flies.<sup>45–51</sup> Furthermore, many of descending neurons (DNs) that relay movement commands from the central brain to the ventral nerve cord (*Drosophila*'s equivalent of a spinal cord) have been identified.<sup>52–54</sup> Functional measurements and perturbations of these populations have identified cell types that can specifically induce forward and backward walking.<sup>55–58</sup> Moreover, characterization of circuits that relay visual information to DNs has provided insights into how vision can monitor self-motion and guide steering control.<sup>59</sup> In addition, targeted studies of specific visual interneurons have revealed how efference copy signals are relayed into the visual system to modulate processing, and large-scale imaging studies have identified substantial ascending signals in walking animals.<sup>60–68</sup> Finally, navigation related neural signals in the central complex, as well as



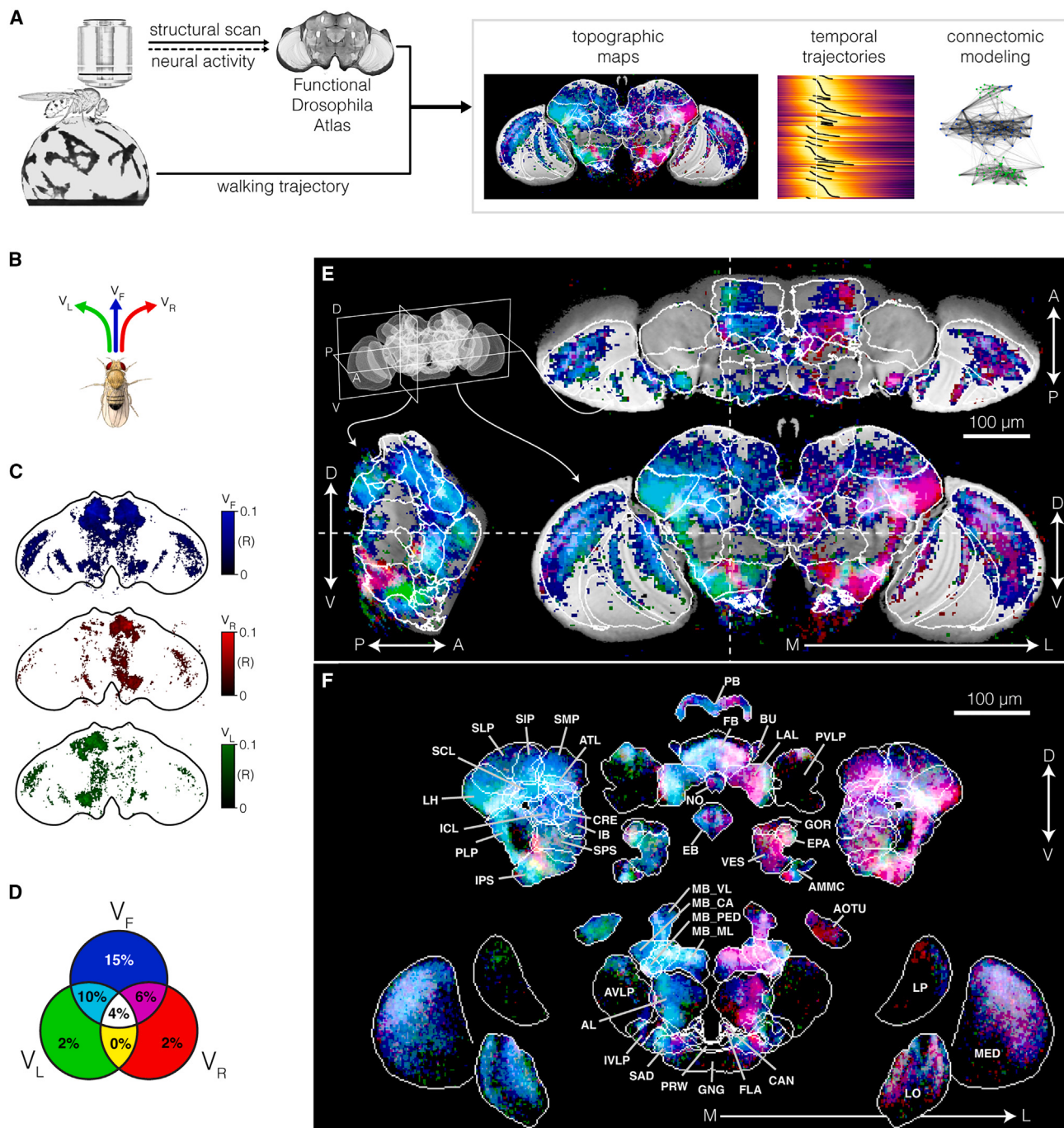


**Figure 1. Mapping the neural representation of walking velocity across the *Drosophila* brain**

(A) The posterior head cuticle is removed to allow optical access to the brain and the fly is secured under a two-photon microscope. The entire volume of the fly brain is imaged at a rate of 1.8 Hz for a 30 min session. All neurons express GCaMP6f to measure neural activity and tdTomato to measure brain structure. Both fluorophores are simultaneously excited and emission photons collected. While imaging, the animal's walking trajectory is recorded. Nine individuals were imaged, and their neural activity was spatially aligned to the Functional Drosophila Atlas by using the structural scan. This dataset was then analyzed to reveal topographic maps of behavior, their temporal trajectories, and their relationship to the connectome.

(B) The trajectory of the fly was decomposed into a continuous forward velocity, as well as positive (clockwise) and negative (anticlockwise) continuous angular velocities.

(C) Correlation map of individual voxels for each behavioral velocity. A single example slice is shown. Voxels above a significance threshold were not considered for analysis and were set to white ( $p > 0.0001$ ; see STAR Methods).

(legend continued on next page)

associative learning signals in the mushroom body (MB), are also modulated by walking.<sup>69–76</sup> However, how these many motor signals might be spatially organized across and within brain regions, and coordinated in time as walking occurs, is unclear.

Here, we use volumetric two-photon imaging to extract neural activity across the entire *Drosophila* brain as the animal behaves. Using this method, we show that the changes in forward and rotational velocity of the animal recruit distinct brain regions whose fine structure reveals detailed topographic structure within individual brain regions spanning tens of microns. We next measure the temporal relationships between neural activity and the execution of movements and observe activity in some brain regions that precedes changes in velocity, whereas activity in other regions lags behind behavior by more than a second. The temporal evolution of this activity thus describes a stereotyped pattern of recruitment of specific brain regions during walking. Combining the fine spatial structure of the topographic map of neural selectivity within individual brain regions with its temporal sequence of activation suggests a spatiotemporal framework for relating neural activity to specific behavioral maneuvers. Because of the fine spatial scale of our topographic maps, we reasoned we could relate the spatial distribution of our signals to underlying neurons. By registering a connectome to our dataset, we show that the maps associated changes in angular velocity are selectively associated with a small, specific population of DNs, as well as a subset of their pre-synaptic inputs. Conversely, maps associated with changes in forward velocity are selectively associated with the motivational circuitry of the MB, including specific dopaminergic neurons (DANs) and MB output neurons (MBONs). Intriguingly, even though the neurons associated with angular and forward velocities are completely distinct, they are nonetheless tightly interconnected, thereby defining a candidate network for the generation and execution of walking. Taken together, these studies identify a brain-wide spatiotemporal topography of walking and relate specific neural circuits and cell types to global dynamics.

## RESULTS

### A novel method for whole-brain imaging in walking

#### *Drosophila*

Our goal was to map neural activity associated with walking across the *Drosophila* brain, to quantitatively compare these signals across individuals, and to develop mathematical models that relate neural and behavioral measurements. To do this, we implemented a pipeline for recording neural activity across the entire volume of the brain while the animal locomotes (Figure 1A). To collect signal simultaneously from every neuron, we pan-neuronally expressed GCaMP6f to monitor neural activity and myristylated-tdTomato as a structural marker.<sup>77,78</sup> Head-fixed flies with a dissected posterior head cuticle were mounted to a two-photon microscope. Resonant scanning was employed to achieve a

volume imaging rate of 1.8 Hz, collecting approximately 1.6 million voxels per volume, each occupying  $2.6 \times 2.6 \times 5 \mu\text{m}$ . Signals from both fluorophores were acquired simultaneously. Each animal was imaged for 30 min while their walking trajectory was measured by recording the rotations of an air-suspended treadmill ball. The experiment was directly followed by collection of a high spatial resolution ( $0.6 \times 0.6 \times 1 \mu\text{m}/\text{voxel}$ ) anatomical scan of the tdTomato signal. These structural measurements allowed us to register every voxel of neural activity across individuals with high spatial accuracy. Previous work generated an *in vivo* Functional *Drosophila* Atlas (FDA), which facilitated the registration of our data into a common space.<sup>79</sup> FDA contains a canonical atlas of labels neuropiles, which we used to parse our data into anatomically defined brain regions. In most subsequent cases, we also reduced the number of features in the neural activity dataset by agglomerative clustering of neighboring voxels with similar responses to create “supervoxels.”

### Neural encoding of velocity space is widespread across the brain

In darkness, tethered flies naturally initiate walking bouts, which include changes in angular velocity and forward velocity, and are interspersed between periods of quiescence and grooming (lasting tens of seconds) (Figure S1; Video S1). We anticipated that in these conditions, neural activity might reveal a common pattern of spatiotemporal dynamics, including signals that initiate movement, execute specific maneuvers, and relay information about ongoing movement to sensory systems. To relate neural activity to behavior, we decomposed the walking trajectories of each fly in the dataset into forward velocity ( $V_F$ ) and rotational velocity ( $V_R$  [right turn, clockwise], and  $V_L$  [left turn, counterclockwise]) (Figure 1B). Then, we calculated the correlation of each voxel’s neural activity with each of these three components (Figure 1C). To visualize the spatial structure of these correlations, we colored the correlation with each velocity component as an axis in red-green-blue (RGB) color space (Figure 1D). Consistent with previous observations, we observed that signals were widespread, with 39% of the brain volume correlating with at least one of the three behavioral variables ( $p < 0.001$ , Bonferroni corrected).<sup>68</sup>  $V_F$  correlations exhibited strong mirror symmetry across the midline and consisted of voxels that correlated only to  $V_F$  (15% brain volume) as well as voxels that correlated with multiple variables (20% brain volume). By contrast,  $V_R$  and  $V_L$  correlations were anti-symmetric, with high levels of correlation on the side of the brain that is ipsilateral to the direction of the turn, with significantly fewer correlated voxels on the contralateral side. In other words, turning to the left (counterclockwise) is strongly correlated with activity in the left hemisphere, and vice versa for a right turn. Most voxels that correlated with  $V_R$  or  $V_L$  also correlated with  $V_F$  (20% brain volume), with relatively few correlating only with turning (4% brain volume). In all, 90% of brain voxels that correlated with behavior displayed a tuning

(D) Venn diagram distribution of voxel tuning types. Voxels were categorically assigned to a velocity set. Numbers indicate percent of voxels in each category. Red, green, and blue correspond to a neural signal that correlated with only one of the three velocity variables, whereas cyan, magenta, and yellow correspond to correlations with two of the variables, and white corresponds to a correlation with all variables.

(E) Example slices through orthogonal planes of the brain. RGB values were independently set based on correlation with velocity components.

(F) Maximum-intensity projection of the partially exploded mean brain illustrating the categorical assignment of voxel tuning (following the color code in D). See also Figures S1 and S2.

preference in velocity space, with only 10% of voxels responding indiscriminately to all velocity components. Taken together, these data argue for the presence of distributed neural signals that relate to specific velocity features of locomotion.

We next wondered how these voxel correlations map onto the anatomical substructures of the brain. Visualizing individual slices through the volume along three orthogonal axes reveals spatially structured correlation patterns, spanning much of the central brain and optic lobes (Figure 1E). However, a 3D representation of this data proved challenging, given the intricate anatomy of the brain. By contrast, cutting the brain into its anatomically defined regions and visualizing them separately allowed the correlations to be visualized well, but the relationships between signals in neighboring neuropils were lost. We therefore split the brain into large regions and then took a maximum-intensity projection through each substructure (Figure 1F). This segmentation revealed that behaviorally correlated voxel signals were highly spatially structured, with some signals being restricted to specific anatomical regions, and others revealing additional structure in which specific layers or subregions of a given anatomical region display selective behavioral correlations.

Although almost all neuropils contained signals that were correlated with behavior, their velocity preferences were highly non-uniform across brain regions (Figures S2A–S2D). To examine the structure of these voxel categories across each anatomical region, we next calculated the fraction of the volume of each anatomical region that was composed of each voxel category. As expected, the central complex navigation and premotor region, including the protocerebral bridge (PB), fan-shaped body (FB), ellipsoid body (EB), and nodulus (NO), was well represented. Similarly, areas that are associated with extensive innervation by DNs, and hence are likely involved in motor control, were also highly engaged, with strong signals in the inferior posterior slope (IPS), superior posterior slope (SPS), vest (VES), superior medial protocerebrum (SMP), and superior lateral protocerebrum (SLP). Notably, however, other regions that also include significant DN innervation are not strongly correlated with walking, suggesting that they may be predominantly engaged in controlling other motor behaviors, for example flying or grooming. Finally, we also observe significant behavioral signals in higher-order sensory areas, including signals related to visual processing (the anterior optic tubercle [AOTU], the lobula [LO], and the medulla [MED]), olfactory processing (antenna lobe [AL] and lateral horn [LH]), and auditory information (antennal mechanosensory and motor center [AMMC]). Finally, the associative learning center, the MB, is also strongly correlated with walking behavior. Taken together, these data demonstrate that locomotor behavior is associated with changes in neural activity across navigation areas, motor areas, higher-order sensory areas, and association areas, revealing the extensive impact of movement on neural processing.

#### Distinct topographic maps of locomotor signals exist in multiple brain regions

This initial characterization revealed that signals associated with specific combinations of forward and angular locomotor velocities were differentially mapped across many brain areas (Figure 1). For example, the IPS, the AOTU, and the VES have a

significant fraction of their volumes occupied by the relatively rare signals associated only with angular velocity (“turning only”); the MB and lateral accessory lobe (LAL) are dominated by the forward-and-turning type; and the SMP and the superior intermediate protocerebrum (SIP) have mostly the forward-only type. We also observed that although ipsilateral hemispheres were well-correlated with turning, there were also notable exceptions, most obviously within subregions of the IPS and LAL, in which contralateral signals were correlated with their respective turn direction.

Given this rich distribution of voxel tuning properties, we next examined whether different voxel signals were spatially organized within each neuropil. Taking slices through orthogonal planes of each neuropil, we observed clear spatial organization at the sub-neuropil scale (Figures 2 and S2E–S2L). The posterior lateral protocerebrum (PLP) contained an approximately 15 μm diameter column of voxels running along the dorsal-ventral axis, which uniformly correlated with both forward and ipsilateral turning velocities (Figure 2A). The IPS contained discrete compartments correlating with either left or right turns and were anti-symmetric between hemispheres (Figure 2B). The LO displayed segregated bands of correlation, consistent with known anatomy, that had mixed selectivity for forward velocity and ipsilateral turning (Figure 2C). The LH contained a dorsal-ventral split, with the dorsal half correlating with forward velocity, and the ventral half correlating with both forward velocity and ipsilateral turning (Figure 2D). The FB contained two distinct layers with identical velocity correlations (forward velocity and ipsilateral turning) (Figure 2E). The entire PB correlated with forward velocity, in addition to an overlaid alternating pattern of left and right turning correlations, matching known functional connectivity (Figure 2F).<sup>80,81</sup> The NO was uniformly correlated with forward velocity but contained distinct glomeruli that correlate with contralateral turning (Figure 2G). Similar to the IPS and the LH, the LAL contained distinct compartments, all correlated with forward velocity, but with the medial portion of the neuropil correlated with ipsilateral turns, and a lateral portion correlated with contralateral turns (Figure 2H). In summary, our experimental and analytical approach has revealed topographic maps containing extensive functional order at the sub-neuropil level, relating neural activity to specific changes in behavior.

#### The temporal relationship between neural activity and behavior varies across brain regions

We next sought to determine the temporal relationship between neural activity and behavior. To do this, we cross-correlated neural activity of each supervoxel with each of the three behavioral variables ( $V_F$ ,  $V_R$ , and  $V_L$ ), sweeping a range of relative time offsets between the two signals. In this analysis, we set  $t = 0$  as the time point at which each behavioral variable changed. Next, at each offset from  $t = 0$ , we calculated the correlation between each supervoxel and each behavioral variable (Figure 3A) and plotted the time of peak correlation for each supervoxel, grouped by brain region (Figures 3B–3D). The results revealed strong spatiotemporal structure across the brain, identifying brain regions whose signals were correlated with future changes in behavior, regions whose maximum correlations were contemporaneous with behavior, and regions that were most correlated with changes in behavior that had happened in the past. At a high

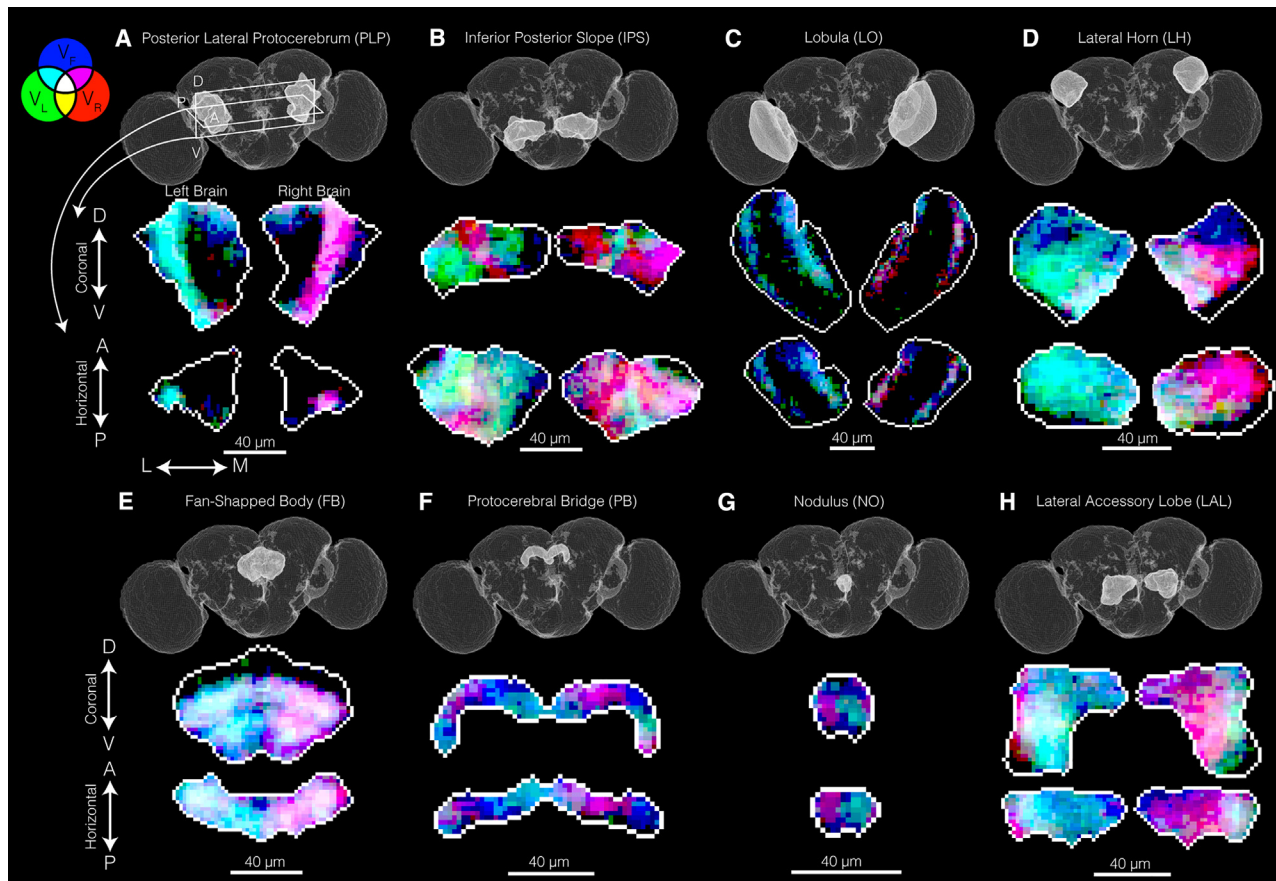


**Figure 2. Topographic maps of neural tuning to behavioral velocities in specific brain regions**

Coronal and horizontal slices shown.

(A) Posterior lateral protocerebrum (PLP).

(B) Inferior posterior slope (IPS).

(C) Lobula (LO).

(D) Lateral horn (LH).

(E) Fan-shaped body (FB).

(F) Protocerebral bridge (PB).

(G) Ellipsoid body (EB).

(H) Lateral accessory lobe (LAL).

Color coding as in Figure 1.

See also Figure S2.

level, the earliest peak correlations between neural activity and behavior emerged in specific neuropils approximately 300 ms before the change in behavior, with the latest peak correlations emerging more than 1 s after the change in behavior. Moreover, these spatiotemporal patterns were different for forward and rotational velocities, consistent with our instantaneous analyses, again suggesting distinct patterns of brain regions are engaged with forward and rotational velocities. In addition, we observed a positive correlation between the time of peak correlation and the width of the temporal kernel, i.e., supervoxels that contain delayed information about behavior displayed a broad temporal kernel, whereas supervoxels that contain anticipatory information about behavior displayed narrow temporal kernels (Figure S3). Thus, lagging signals do not appear to capture as much temporal precision as leading signals and instead reflect integration over a longer history of behavior. Finally, we

emphasize that these time intervals reflect peak correlations rather than the time at which correlations first become statistically significant, thereby establishing a conservative estimate of the interval over which correlations between neural activity and behavior can be detected.

For changes in forward velocity, the earliest peak correlations appeared simultaneously in the LH, the superior intermediate protocerebrum (SIP), the MB, and the AL (Figure 3B). Soon afterward, specific areas associated with extensive DN innervation, such as the gnathal ganglion (GNG) and the saddle (SAD) also display peak correlations with future changes in forward velocity, correlations that can persist until after the change in velocity has occurred. The central complex (including the PB, the FB, the EB, and the NO) also include subregions that have peak correlations that span the initiation of movement but also persist after the correlated change in forward velocity. Finally, peak correlations

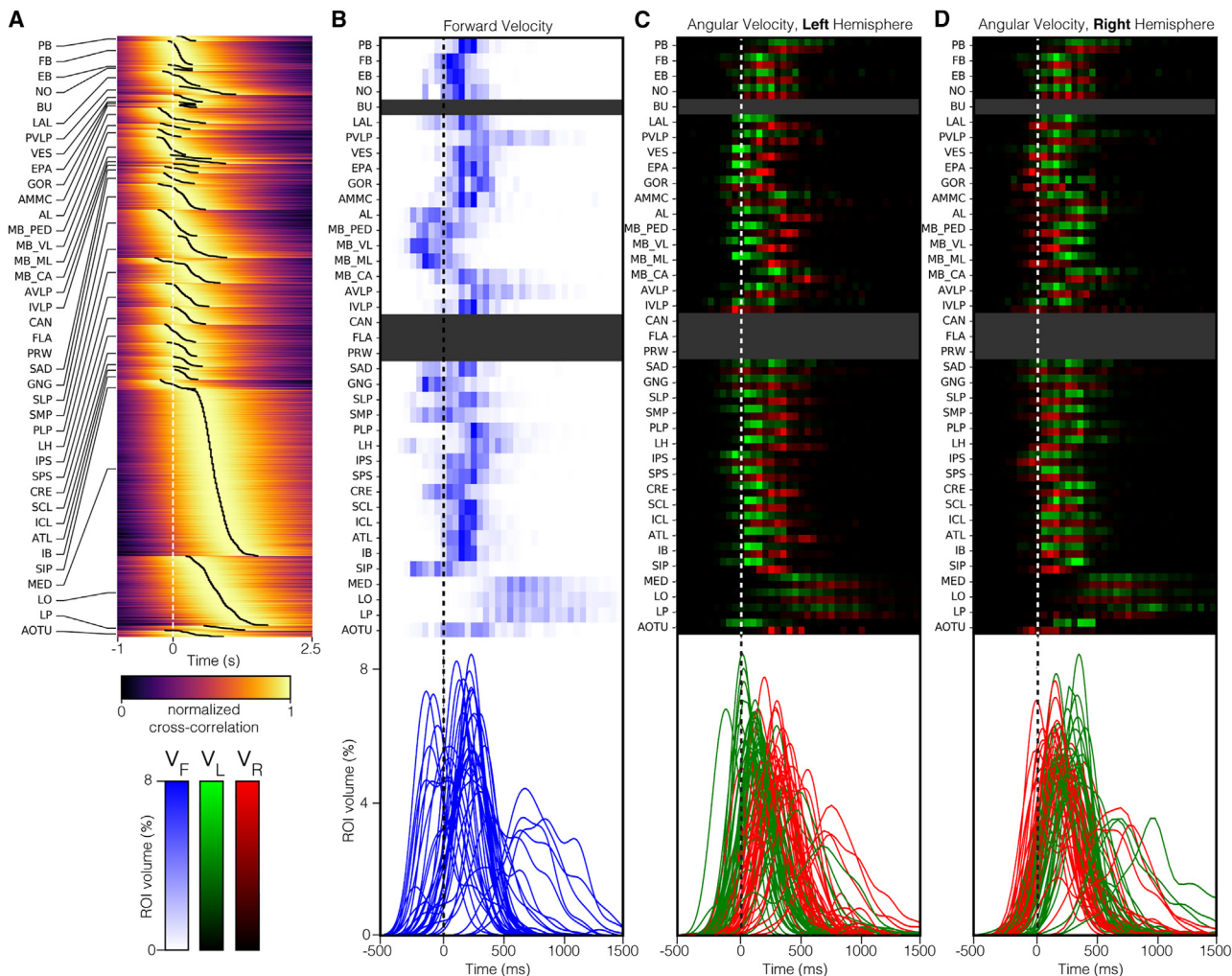


**Figure 3. The temporal relationship between neural activity and behavior varies across brain regions**

(A) Cross-correlation filters of supervoxel neural activity and forward velocity ( $n = 9$  flies). Filters are first sorted by anatomical region, then peak time. Peak times are marked by the black traces. Filters are an average of both hemispheres and have been deconvolved based on measurements of the impulse response of GCaMP6f kinetics (see STAR Methods).

(B) Histograms of peak cross-correlation of supervoxel neural activity and forward velocity. For each anatomical region, the percent of the volume that peaks at a given time is plotted. Below, kernel density estimates from each region are overlaid.

(C) As in (B), but left and right rotational velocities for the left hemisphere.

(D) As in (B), but left and right rotational velocities for the right hemisphere. See also Figure S3.

in sensory areas like the visual system, including the MED and the LO, as well as the lobula plate (LP), emerged only after the change in velocity, and persisted in some cases for more than a second. Thus, changes in forward velocity are correlated with a characteristic sequence of changes in neural activity distributed widely across the brain, spanning sensory, motor, and navigation centers.

A different temporal sequence was observed when neural activity in each supervoxel was correlated with angular velocity (Figures 3C and 3D). In this case, although neural activity in olfactory regions as well as the MB continued to correlate with future changes in angular velocity, a set of motor areas that partially overlapped with those associated with forward velocity but was nonetheless distinct, including the IPS, the gochet (GOR), and the VES, were also correlated with future movements.

Correlations between angular velocity and supervoxels in navigation centers, namely the PB, the FB, the EB, and the NO, lagged changes in velocity, consistent with the fact that these regions can integrate angular velocity signals to represent heading.<sup>81–87</sup> Signals in the optic lobes, the MED, the LO, and the LP, substantially lagged the correlated change in angular velocity. In addition, across nearly all brain regions, the time of peak correlation with angular velocity emerged first in the ipsilateral hemisphere relative to the contralateral hemisphere. We note that maps of the correlations between neural activity and acceleration and deceleration show nearly identical temporal patterns to those seen using velocity (Figure S3). Finally, these temporal kernels are dominated by bona fide walking bouts rather than small ball movements, as thresholding behavior to 0.75 SD (1.8 mm/s for  $V_F$  and 60°/s for  $V_R$ ) had little effect on the observed filters.

### Individual brain regions display spatiotemporally structured patterns of engagement

Given the observation that individual brain regions contained topographic maps of behavioral variables, we next examined whether the distribution of peak correlation times we observed within a region might reflect spatiotemporal trajectories within each topographic map (Figures 4 and S4). These analyses revealed that even within each brain region, the temporal order of neural engagement was highly organized and aligned with both behavioral and anatomical features. For example, the LH contains a dorsal region that was more correlated with forward velocity, and a ventral region that was more associated with angular velocity (Figure 4). For forward velocity, this functional division corresponds to a temporal separation, with the dorsal region being correlated with behavior before the ventral region. Conversely, for angular velocity, this functional division is erased: on the ipsilateral side, most of the LH displayed early correlations with the change in velocity, whereas on the contralateral side, peak correlation times gradually progressed along the medial-lateral axis. Indeed, such temporal gradients were widespread across brain regions, across different axes, and correlated with either forward or angular velocity, being apparent in the IPS, the SMP, the SIP, and the FB. In other brain regions, such as the LAL, the MB medial lobe (MB-ML), and the PLP, the timing of peak correlations with forward velocity was uniformly distributed across the structure, whereas the timing of peak correlations with angular velocity displayed the characteristic temporal order of ipsilateral signals preceding contralateral signals. Finally, in the optic lobe, where all of the correlations with behavior presumably reflect feedback entering the visual system from the central brain, the temporal order of activation captured the ipsi-leading, contra-lagging pattern for angular velocity and mapped onto distinct “input” layers.

### Demixing the unique contribution of each velocity component to neural activity

The structure of walking behavior produces correlated changes in forward and angular velocities over a wide range of time-scales.<sup>44,49</sup> Such behavioral correlations can obfuscate the relationship between neural activity and a specific behavioral variable. To estimate the effect of such correlations, we built a linear model that predicted neural activity in each voxel using four separate behavioral variables, namely a binary variable describing locomotor state (walking or stopped), forward velocity, and left and right angular velocities (see STAR Methods). Using this approach, we distinguished between the variance of each voxel that could be explained by several behavior variables versus the *unique* variance of the voxel that could be explained only by one specific variable. That is, we identified neural activity signals that could not be accounted for using any of the other three behavior variables and were therefore unique on a voxel-by-voxel basis.

Using this approach, we reconstructed brain-wide maps of the contributions of each voxel to each single variable trained separately, as well as of the unique contributions of each of the four behavioral variables, trained together (Figure 5A). This comparison revealed that the brain-wide maps of unique contributions identified sparser subsets of voxels than the single variable models (Figure 5A). For example, although the single variable forward walking and locomotor state (stopped versus walking)

maps were very similar, the maps created by demixing revealed that forward velocity was encoded by a spatially organized subset of voxels, whereas locomotor state was not encoded uniquely anywhere in the brain.

As the unique contributions of forward velocity and left and right angular velocities revealed clearly distinct spatial networks, we wanted to more closely examine these functional regions and their tuning properties (Figures 5B–5E). To do this, we averaged neural activity across each of the functional brain regions and plotted their relationships to each of the three behavioral variables (Figure 5B). As before, we set a velocity threshold to approximate the speed at which a fly transitions between walking and not walking. Then, we calculated the correlation between each functional region and each velocity component, separately for below and above the threshold (Figure 5C). Significantly, we found that all three regions were highly correlated when the fly was stopped (below the threshold), strongly arguing for a widespread increase in neural activity associated with the initiation of movement (Figure S5). Moreover, when moving (above the threshold), each brain region had a different response to each of the three velocity variables, and as expected, each region had strong correlations with only one behavioral velocity component (Figures 5D and 5E). Overall, this analysis has allowed us to spatially define functional brain regions that relate to unique axes of velocity space. This decomposition will assist the following analysis of relating these distinct maps to the underlying neural networks.

### Registering functional signals to the connectome

Previous work generated an atlas, the FDA, in which the anatomy of the *in vivo* brain was registered to the anatomy of the *ex vivo*, fixed brain that contains the “hemi-brain” connectome.<sup>79</sup> By aligning our functional imaging dataset to the FDA, we could assign individual voxel to locations of specific neurites and synapses in the connectome with a spatial resolution of approximately 5 μm.<sup>79</sup> However, as each voxel spans 2.6 μm × 2.6 μm × 5 μm, it typically contains neurites from approximately 10 neurons, making the assignment of unique neural sources to an individual voxel signal ambiguous. However, because each neuron spans a large volume, its contribution to the functional signal will be distributed across many voxels. As functional signals sharing a common relationship to behavior span thousands of voxels, we hypothesized that we could identify candidate source neurons whose spatial distribution of synapses aligns with the positions of voxels with similar behavioral signals.

As an initial assessment of whether our functional recordings have any relationship to the connectome, we asked if voxels that contain information about behavior are more strongly connected to each other in the connectome than expected by chance. To define a null distribution that captures the relationship between distance and connectivity, we set a range of Euclidian distance bins and, for each, generated a bootstrapped distribution of connectivity (defined by the number of synapses per unit volume) of voxels within the bin across the entire hemi-brain (Figure S6). This analysis revealed that voxels that were 5 μm apart displayed an average normalized connection strength of 0.71, whereas voxels that were 100 μm apart have an average normalized connection strength of 0.01 (see STAR Methods). By contrast, if the voxels were first filtered to include only voxels

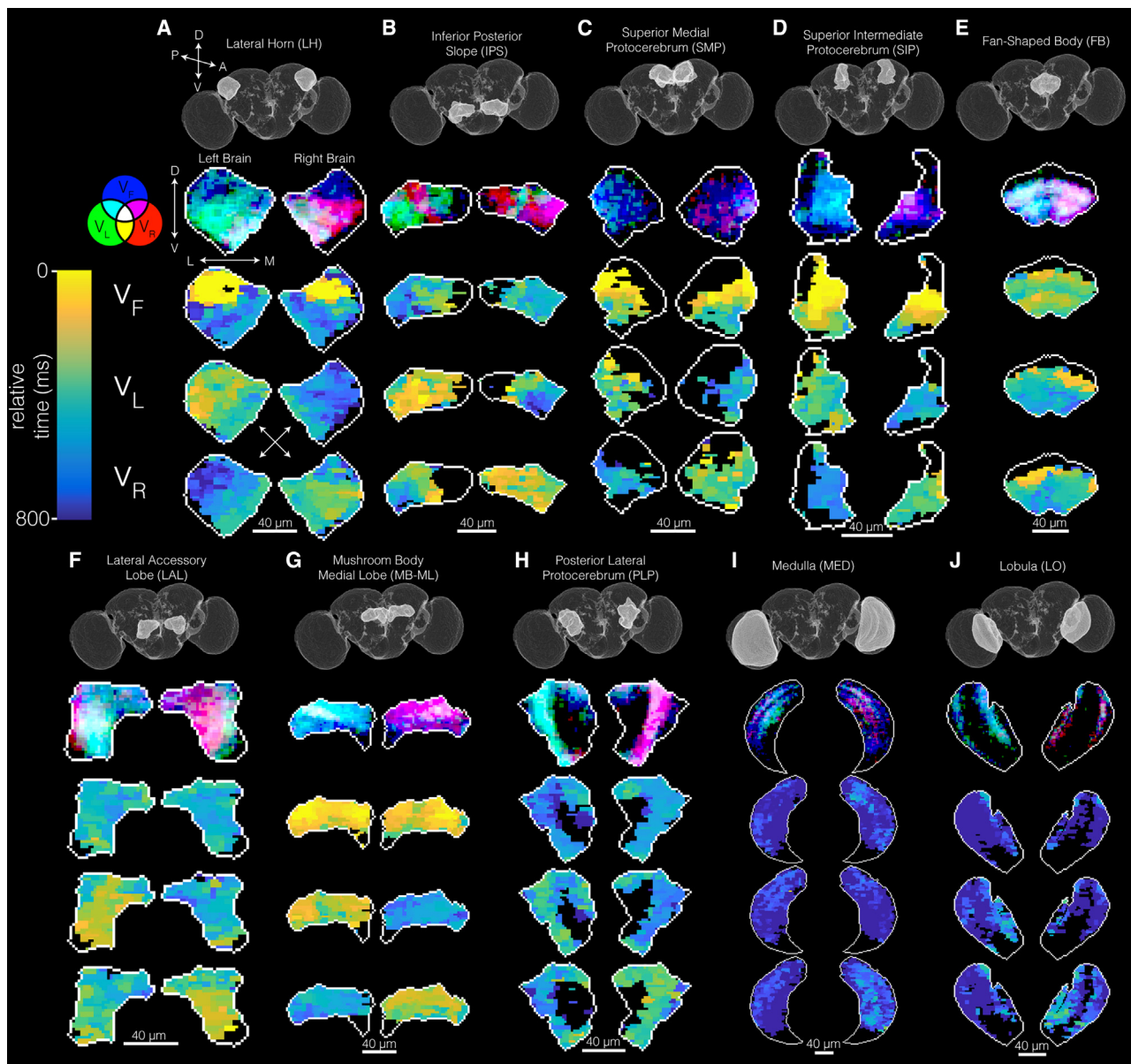


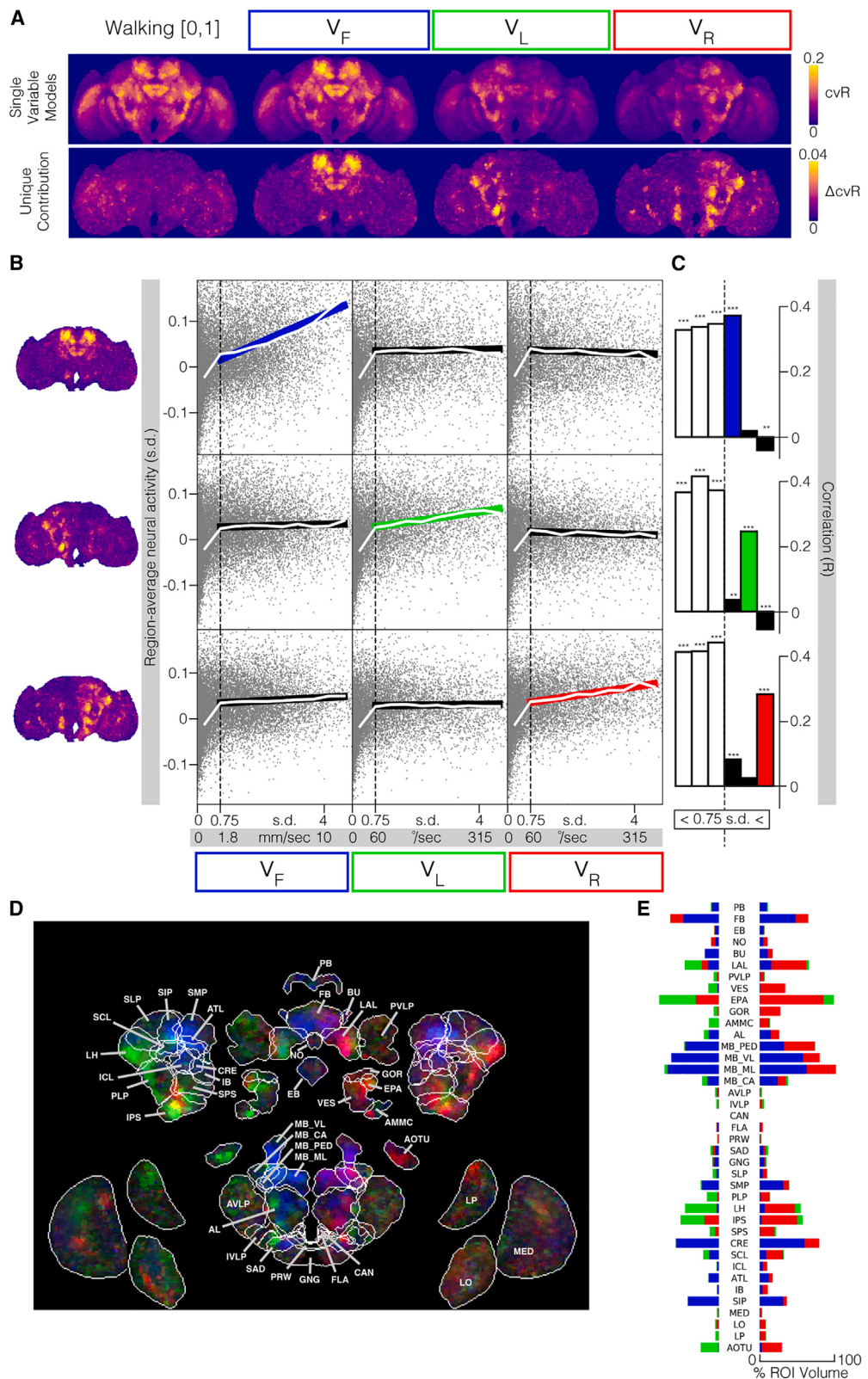
**Figure 4. Topographic maps of peak correlation times are spatially structured within individual brain regions**

- (A) Lateral horn (LH).
  - (B) Inferior posterior slope (IPS).
  - (C) Superior medial protocerebrum (SMP).
  - (D) Superior intermediate protocerebrum (SIP).
  - (E) Fan-shaped body (FB).
  - (F) Lateral accessory lobe (LAL).
  - (G) Mushroom body medial lobe (MB-ML).
  - (H) Posterior lateral protocerebrum (PLP).
  - (I) Medulla (MED).
  - (J) Lobula (LO).
- Each column contains the correlation maps describing the behavior correlation strength (from Figure 2), as well as the topographic maps of relative peak correlation time for  $V_F$ ,  $V_L$ , and  $V_R$ .

See also Figure S4.

that have a Pearson's correlation above 0.2 to angular velocity, they displayed a much higher connection strength of 6.33 and 0.18, respectively (Figure S6). A similar pattern was seen when we selected for voxels that were significantly correlated with

forward velocity and were maintained across a wide range of distance bins. Thus, both the forward and rotational velocity topographic maps correspond to neurons that are more highly synaptically connected than expected by chance.



(legend on next page)

As a proof of concept for identifying candidate source neurons underlying our functional signals, we first examined the neuron type most directly linked to controlling ipsilateral turning, the DN DNA02.<sup>58</sup> We constructed two 3D binary masks to facilitate this analysis: a “neuron mask,” which labeled all voxels containing DNA02 synapses, and a “behavior mask” which labeled all voxels containing a neural signal uniquely correlated with ipsilateral turning (above a threshold of  $r = 0.01$ ; **Figure 6**). We calculated the Sørensen-Dice coefficient of overlap between these two masks as 0.0931, compared with an average of 0.0043 for randomly selected neurons. To estimate the significance of these scores, we next calculated the Sørensen-Dice coefficient for each of the 24,691 neurons in the hemi-brain (**Figure 6B**). As expected, most neurons had very low Sørensen-Dice scores, with a small tail of neurons with exceptionally high Sørensen-Dice scores (**Figure 6B**). Strikingly, DNA02 was the 6<sup>th</sup> highest-scoring neuron in the dataset (0.024% percentile). Moreover, although DNs are distributed across the central brain, we found that overall our behavioral maps were highly enriched for specific DNs (**Figures 6B** and **S6C**), with particularly high Sørensen-Dice scores associated with DNA04, DNA03, and DNb01, corresponding to ranks 21, 24, and 31 out of 24,691 neurons, respectively. Given that the distribution of Sørensen-Dice coefficients is highly skewed toward specific cell types, including the one DN known to have a very strong relationship to ipsilateral turning, we infer that our approach can accurately identify candidate neurons associated with specific functional signals.

#### Identification of neural networks associated with walking

Given that functional voxels with similar relationships to behavior were more highly synaptically connected than expected by chance (**Figure S6**) and that no single neuron could account for a large fraction of the functional signals, we reasoned that the spatial distribution of neural signals must emerge from a network. To identify these candidate networks, we first calculated the percent of each neuron’s synapses that were contained within a particular behavior mask. We then employed a 2D-grid search (**Figure 6C**) that first swept across a range of thresholds for percent synapses in the behavior mask and then pruned this list by sweeping across a connectivity threshold (see **STAR Methods**). Within the resulting 2D space, we computed isocontours for two variables: the number of neurons in the network and the network Sørensen-Dice score (**Figures 6C** and **S7**). We observed smooth gradients and only one local minimum for each variable, demonstrating that our approach converged on a single grid region. In parallel, we repeated this procedure, except instead of using the percent of

synapses in the mask as the grid search initializer, we used each neuron’s Sørensen-Dice coefficient (**Figures S7B** and **S7D**). Finally, we intersected the networks identified by both grid search procedures and selected neurons common to both (**Figure S6D**). This procedure identified a small subnetwork of neurons that were highly interconnected, covered a high fraction of the behavior map, and whose constituent neurons overlapped highly with the behavioral mask.

Using this approach, we identified the networks associated with changes in angular and forward velocity (**Table S1**). We then embedded the 48 cells in the ipsilateral turning network and the 54 cells in the forward velocity network within the same force-directed spring graph to visualize the structure of these networks and their connections (**Figures 6D** and **S6E**). We found the turning subnetwork comprised two distinct subnetworks that were bridged by a single forward velocity subnetwork. One of these turning subnetworks spanned motor regions, including the LAL, the IPS, and the SPS, and contained five DNs, whereas the other turning subnetwork covered a sensory processing and association region, the LH, and contained no DNs. Strikingly, although the turning and forward networks extend over substantially different regions of the brain (**Figures 1** and **5**), the two networks are nonetheless highly interconnected, identifying candidate cells that enable these two behavioral signals to interact to guide walking.

#### Identifying specific candidate neurons for circuit dissection

In addition to describing the network architecture, our approach identified specific candidate neurons for subsequent analysis. The forward velocity network contained thirteen MBONs, four DANs, five crepine neurons (CRE), five SMP neurons, and three LH neurons (**Figure 6E**). Previous work has demonstrated a role for DANs and MBONs in guiding goal-directed walking behavior, as well as a previously hypothesized role for the CRE and the SMP in collecting these MBON signals and relaying them to motor circuits.<sup>69,72,88</sup> Furthermore, our network is enriched for aversive MBONs, presumably reflecting the state of the fly during imaging. Finally, we identified an octopaminergic neuron, OA-VPM3, consistent with octopamine release during walking.

Of the five DNs in the turning network, we focused on the three with substantial connectivity with other neurons in the network: DNA02, DNA03, and DNA04 (**Figure 6F**). These DNs receive hundreds of synaptic inputs from many cells in the network, with substantial overlap in their synaptic inputs. This DN input layer was also highly interconnected, suggesting that turning reflects the action of a complex network. Finally, we note that diverse neuropils provide input to this network, including some primarily

**Figure 5. Demixing the unique contributions of each velocity component to neural activity using linear models**

(A) Cross-validated linear models fit to predict voxel activities given various behavior input features. Maximum projections of R prediction accuracy are shown. Top row: models are given only one behavior variable. Bottom row: the unique contribution of each behavior variable is measured by comparing a model that receives all four behavior variables to one that receives all variables except for the variable of interest.

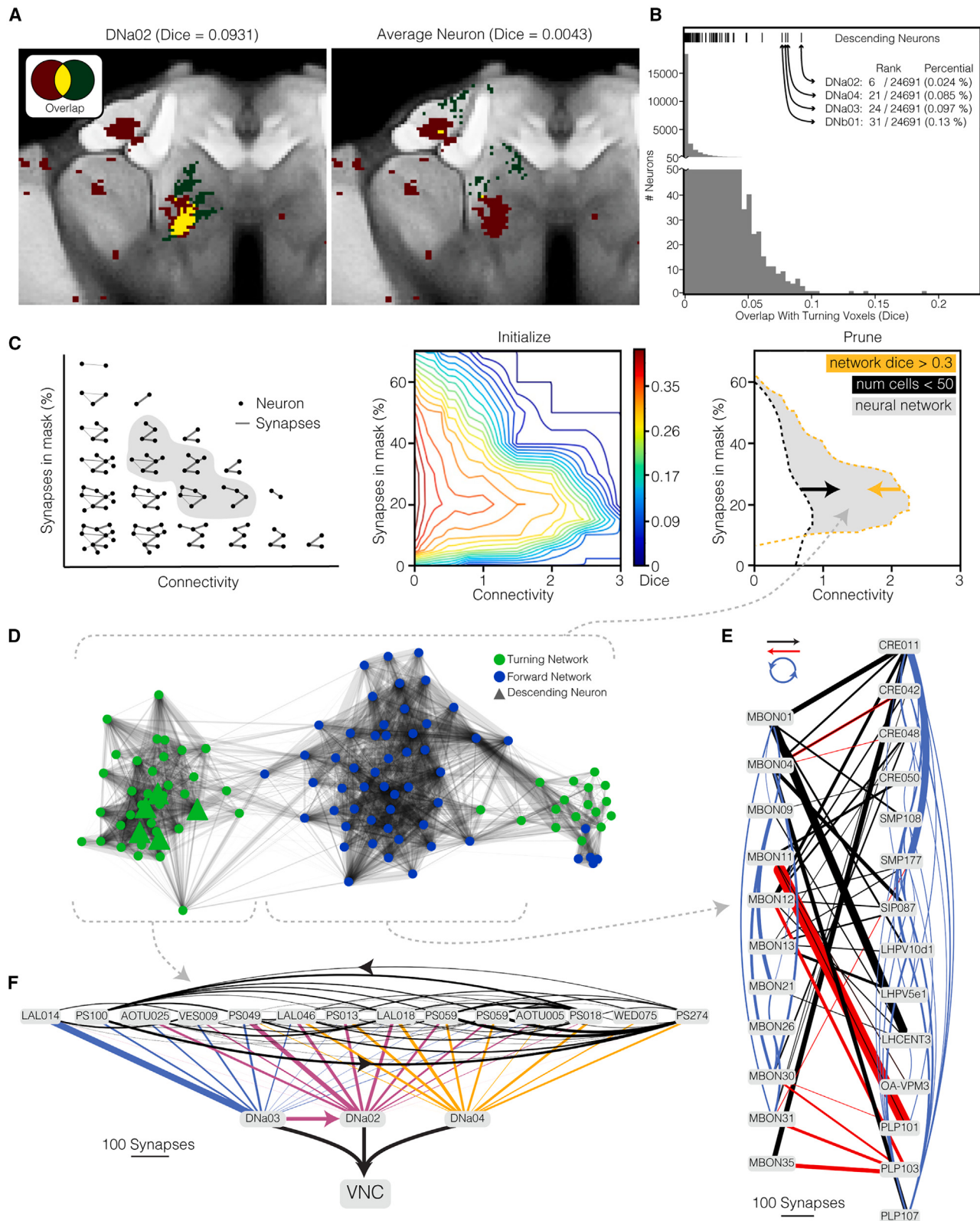
(B) Relationship between mean neural activity across identified functional regions from (A) versus each behavioral variable. Gray dots are single time points. The vertical dashed black line represents the threshold between moving and not moving (1.8 mm/s for forward velocity and 60°/s for rotational velocity). Colored lines and thick black lines are the linear regression of data above threshold. White lines are mean bin values, with width of 0.5 SD. Vertical white lines represent  $\pm 1$  SEM but are too small to be visible.

(C) Quantification of data in (B). Correlations were measured independently below and above the movement threshold. \* $p < 0.05$ , \*\* $p < 0.01$ , \*\*\* $p < 0.001$ .

(D) Maximum-intensity projection colored by functional regions defined in (A).

(E) Percent of voxels in each anatomical region of interest (ROI) that fall into each functional region.

See also **Figure S5**.



(legend on next page)

associated with sensory processing, most notably the AOTU for visual input, and the wedge (WED) for mechanosensory input. Thus, this control network is likely integrating information from across sensory neuropiles to guide behavior, and our analysis has identified the specific neuron candidates that are likely to mediate these interactions across neuropiles.

## DISCUSSION

Here, we describe a two-photon imaging approach to extract neural signals across the entire *Drosophila* brain as the animal behaves, and via volumetric registration, quantitatively compare signals across brain regions and individuals (Figure 1). We find that neural activity containing information about locomotion is widespread across the brain, extending well beyond regions commonly associated with motor control, in line with previous results (Figure 1).<sup>68</sup> We observe striking topographic order within individual brain regions, such that neurons with similar selectivity for behavioral features are grouped together (Figure 2). We find that the temporal relationship between neural activity and behavior evolves across the brain: activity in some regions precedes changes in locomotor velocity by 300 ms; in others, changes in neural activity are contemporaneous with behavior, whereas in others, neural activity lags behavioral changes by more than a second (Figure 3). Within many individual brain regions, we observe temporal gradients of neural activity that sometimes respect functional compartments but more often sequentially engage neurons with different behavioral selectivity (Figure 4). By registering a connectome to our dataset, we related the spatial topography of our forward and rotational velocity signals to networks of specific candidate neurons (Figures 5 and 6). Taken together, these studies identify a brain-wide spatiotemporal topography of walking in which distinct networks of neurons are engaged by specific behavioral maneuvers and follow stereotyped temporal trajectories.

### Locomotor signals are widespread and highly structured

Measurements and perturbations of genetically identified cell types have provided fundamental insights into a wide diversity of neural processes in the fruit fly. At the same time, how these relatively compact circuit computations might be embedded within larger neural networks that could be engaged during behavior has remained unclear. Our data, and other recent work using different large-scale imaging approaches,

demonstrate that locomotor signals can be detected in approximately 40% of the brain volume and across almost every neuropil (Figure 1).<sup>35,68</sup> The selectivity of these signals to specific behavioral variables is spatially structured, even within individual brain regions, well above the spatial resolution of our imaging approach (Figure 2). Given the scale of these motor maps relative to the size of individual neurons and their processes, this observation demonstrates that neurons that have similar tuning with respect to locomotor behavior are physically grouped.

These distributed locomotor signals likely play diverse computational roles in different brain regions. For example, modulation of visual circuits by locomotion-evoked changes in octopamine increase the gain of visual processing to capture the more rapid changes in visual scene statistics caused by movement.<sup>66</sup> In addition, locomotion can provide a predictive signal that can incorporate the dynamics of locomotor behavior to modulate motion processing.<sup>61–64,89</sup> Consistent with these previous observations, our data reveal extensive locomotor signals in the visual neuropils, including the MED, LO, and LP, and are often restricted to specific processing layers (Figure 2). We note that we were unlikely to directly detect rapid efference copy signals that hyperpolarize specific visual interneurons given that we were imaging GCaMP6f, which favors depolarizing signals.<sup>62–64,77</sup>

Beyond early visual processing, behavior signals have been previously observed in higher-order circuits. In particular, the MB, responsible for learning and memory in *Drosophila*, encodes behavior as a dopaminergic signal to coordinate synaptic plasticity and reward.<sup>69,72</sup> In addition, navigation circuits in the EB rely on behavior evoked signals to coordinate remapping of the heading-direction network.<sup>70</sup> Moreover, the FB, another region engaged with sensory integration and navigation, shows behavior-based gating of visual responses.<sup>71</sup> Our data, and other recent work, extend these observations to many other regions in the central brain that have had only limited functional characterization, opening new avenues for understanding the interactions between behavior and other circuit computations.<sup>35,68</sup> Finally, the breadth and diversity of the locomotor signals we describe in the fly closely parallel analogous observations in a variety of contexts and brain regions in other animals.<sup>16</sup>

### Different locomotor movements engage distinct spatiotemporal neural networks

Locomotor behavior reflects complex, time-evolving changes in specific velocities that are structured over hundreds of milliseconds.<sup>44–51</sup> Our data demonstrate that changes in the

**Figure 6. Identifying the neural networks underlying topographic maps of forward and rotational velocities**

- (A) A single slice through the Functional *Drosophila* Atlas. Red voxels indicate rotational velocity signal, as determined by the unique variance explained analysis. Green voxels contain synapses from an example neuron, DNa02 (left), and X (right). Yellow voxels are the overlap. DNa02 provides an example of unusually high overlap, whereas X has an average overlap, as calculated by the Sørensen-Dice coefficient.
- (B) Histogram of overlap of each neuron in the hemi-brain connectome with the rotational velocity map. Tick marks indicate the position of each descending neuron, which are highly enriched within the rotational velocity map (Figure S6C).
- (C) 2D-grid-search strategy for identifying the underlying neural network (STAR Methods). Candidate networks are first initialized by sweeping across a range of thresholds for percent of a neuron's synapses within the mask. This is followed by pruning by sweeping across connectivity within the network and rejecting all networks that are composed of either too many neurons or have too low of a network dice score (STAR Methods).
- (D) A force-directed spring network diagram of the identified networks.
- (E) Schematic of neurons in the forward velocity network, emphasizing the enrichment of MBONs and their inputs and outputs. Black lines are MBON output synapses, red lines are MBON input synapses, and blue lines are synapses between MBONs and between non-MBONs.
- (F) Schematic of neurons in the rotational velocity network, emphasizing their convergence onto three DNS.

See also Figures S6 and S7 and Table S1.

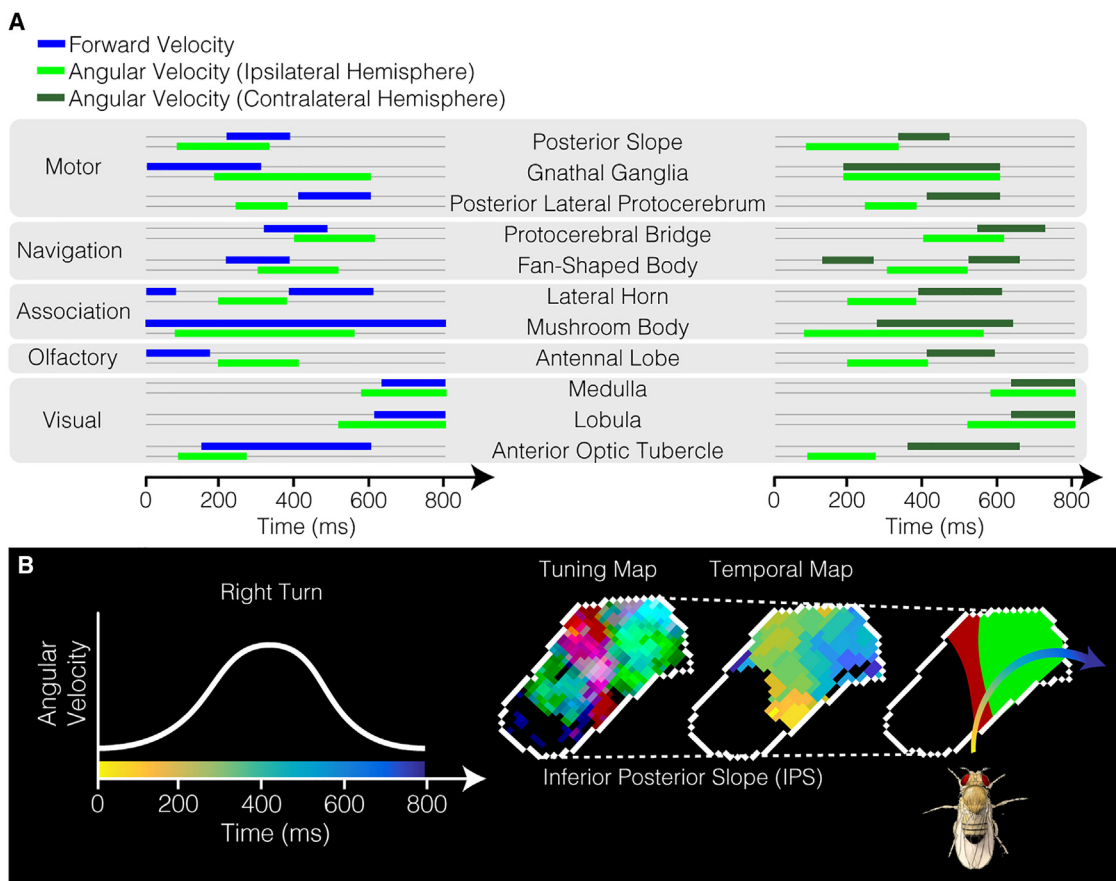


**Figure 7. Locomotion related signals are temporally ordered within and across brain regions**

(A) Representation of categorized brain regions activating and deactivating along a temporal sequence. Comparing forward and angular velocity, as well as insilateral and contralateral hemispheres for angular velocity.

(B) Abstract representation of how a motor region with compartmentalized velocity tuning combined with a temporal gradient of neural activity could embed a stereotyped behavioral maneuver, such as a turn.

instantaneous forward and angular velocities of the animal engage distinct neural networks distributed over multiple brain regions and follow stereotyped temporal sequences of coordinated activity (Figures 3 and 4). Focusing on neural signals that anticipate and are contemporaneous with changes in behavioral velocities reveals engagement of regions that contain substantial innervation by DNs, a key bottleneck in motor control, as well as other regions whose relationship to motor control is unknown. Our results demonstrate that the temporal relationships between neural signals in each brain region and changes in specific behavioral velocities are exceptionally rich and reflect multiple levels of functional and anatomical organization (Figures 3 and 4). Strikingly, temporal gradients of correlation that presumably reflect wave-like sequences of changes in neural activity that propagate across specific regions are a common organizational principle in this system (Figure 7). Thus, understanding how temporal patterns of DN recruitment and dismissal emerge will likely require relating these patterns to the extensive networks in which they are embedded. Finally, we note that the temporal structure of walking includes faster timescales, such as those associated with saccades or individual steps, signals that our approach would likely have missed and could be revealed in future work.

## Bridging brain-wide activity to networks and neurons

Large-scale neural recordings are of rapidly expanding interest across model systems. In most cases, relating these population dynamics to specific cell types is challenging. We developed a quantitative method that systematically determines the network of neurons most likely to underlie an observed spatial pattern of neural activity. By precisely aligning a connectome containing neural identities and synaptic locations to our functional imaging dataset, we extracted candidate neural networks underlying our brain-wide recordings. Like transcriptomic, proteomic, and genetic screens, this approach seeks to provide an initial list of candidates, which can then be explored in more detail using targeted strategies. More broadly, this approach is particularly valuable for behaviors whose circuit basis may be entirely unknown, as voxels with significant behavioral correlations identified using whole-brain imaging can be used to establish toeholds into circuits via connectome registration.

We first demonstrate that our measured topographic maps correspond to structure in the connectome (Figures S6A and S6B). Next, we found that the network that correlates with changes in angular velocity converged on five DNs, including three that were highly interconnected with other components

of the network: DN<sub>a</sub>02, DN<sub>a</sub>03, and DN<sub>a</sub>04. Previous work had identified DN<sub>a</sub>02 as playing a critical role in controlling turning, making DN<sub>a</sub>03 and DN<sub>a</sub>04 promising candidates for subsequent analysis. The identified inputs to these were distributed across multiple neuropiles, including the LAL, the IPS, the WED, and the AOTU. Consistent with a role for these input neurons in controlling rotational velocity, functional signals in these neuropiles preceded changes in turning behavior. Overall, these results support a conceptualization of rotational velocity control by individual neurons distributed across the brain converging on a small population of specific DNs. Finally, we note that an NBLAST-based analysis demonstrated that these neurons cannot be replaced by alternative neurons with similar morphology without a reduction in Sørensen-Dice and network synapse counts, further suggesting these identified neurons as promising candidates for further dissection (see STAR Methods; Figure S7).<sup>90</sup>

In contrast to the rotational velocity network, the forward velocity network contained no DNs. Rather, this network centered on the MBONs, and a set of their inputs and outputs, including specific dopaminergic PPL neurons. Importantly, previous studies have demonstrated that both MBONs and PPL neurons contain walking related signals.<sup>69,72,88</sup> Our temporal maps indicate that the voxels and brain regions that contain these neurons precede changes in forward velocity by 300 ms, consistent with their known motivational role. Additionally, the subset of identified MBONs and DANs we identified were enriched for those known to have negative valence associations, suggesting that in the context of our experiments, the animals were motivated to escape.<sup>91</sup> Finally, we note that because the hemi-brain does not include the GNG, there may be additional neurons that we could identify.

Overall, the fine structure of our spatiotemporal maps suggests a framework for how neurons with different feature selectivities can be sequentially engaged during a movement trajectory (Figure 7). In particular, although the processes of neurons with similar selectivities are spatially clustered, the temporal precession of neural activity is often spatially graded and can cross more than one cluster. This suggests that different pools of neurons are recruited in a specific temporal order that relates to the evolving pattern of movement. By aligning a connectome to our dataset, we reveal the neural network underlying these topographic maps and identify specific neural substrates that can be studied in subsequent studies. Given the powerful tools available in the fly for targeted measurements and perturbations, *Drosophila* is now well poised to reveal additional principles by which local circuits and single cells interact across brain-wide networks to guide neural and behavioral dynamics.

### STAR★METHODS

Detailed methods are provided in the online version of this paper and include the following:

- KEY RESOURCES TABLE
- RESOURCE AVAILABILITY
  - Lead contact
  - Materials availability
  - Data and code availability
- EXPERIMENTAL MODEL AND SUBJECT DETAILS

### ● METHOD DETAILS

- Mounting and dissection
- Two-photon imaging
- Behavior tracking
- Data preprocessing
- Data alignment

### ● QUANTIFICATION AND STATISTICAL ANALYSIS

- Agglomerative clustering supervoxel creation
- Correlation analysis (voxel- and supervoxel-wise)
- Unique variance explained modeling
- Cross-correlation analysis
- GCaMP6f deconvolution
- Registration of connectome to functional data
- Parcellation of functional data for comparison to connectome
- Connectivity of functional regions
- Identification of neural networks underlying functional signals
- Comparing identified neurons with next most similar candidates

### SUPPLEMENTAL INFORMATION

Supplemental information can be found online at <https://doi.org/10.1016/j.cub.2023.12.063>.

### ACKNOWLEDGMENTS

We would like to thank members of the Clandinin Lab, as well as Diego Pacheco, Osama Ahmed, and Salil Bidaye, for feedback on the manuscript. We would also like to thank the Dickinson lab for providing us with treadmill balls and Bob Schneeveis for manufacturing mounting parts. This work was supported by a National Science Foundation Graduate Research Fellowship (B.E.B.), grants from the NIH (R01EY022628, 5U19NS104655 [T.R.C. and S.D.], and 3R01NS11006003 [T.R.C.]), the Stanford Vision Core Grant (5P30EY02687704 [T.R.C.]), and the Simons Foundation (T.R.C.).

### AUTHOR CONTRIBUTIONS

B.E.B. and T.R.C. conceived the project. B.E.B. collected experiments and analyzed the data. A.B.B. and Y.A.H. registered neural data. F.C. computed the adjacency matrix of supervoxel connectivity based on the connectome. S.D. provided modeling direction and feedback. B.E.B. and T.R.C. wrote the manuscript. T.R.C. advised throughout the project.

### DECLARATION OF INTERESTS

The authors declare no competing interests.

Received: August 16, 2023

Revised: November 13, 2023

Accepted: December 20, 2023

Published: January 18, 2024

### REFERENCES

1. Kaas, J.H. (1997). Topographic maps are fundamental to sensory processing. *Brain Res. Bull.* 44, 107–112.
2. Leyton, A.S.F., and Sherrington, C.S. (1917). Observations on the excitatory cortex of the chimpanzee, orang-utan, and gorilla. *Q. J. Exp. Physiol.* 11, 135–222.
3. Patel, G.H., Kaplan, D.M., and Snyder, L.H. (2014). Topographic organization in the brain: searching for general principles. *Trends Cogn. Sci.* 18, 351–363.

4. Malin, J., and Desplan, C. (2021). Neural specification, targeting, and circuit formation during visual system assembly. *Proc. Natl. Acad. Sci. USA* **118**, e2101823118.
5. Churchland, M.M., Cunningham, J.P., Kaufman, M.T., Foster, J.D., Nuyujukian, P., Ryu, S.I., and Shenoy, K.V. (2012). Neural population dynamics during reaching. *Nature* **487**, 51–56.
6. Graziano, M.S.A., and Afalo, T.N. (2007). Mapping behavioral repertoire onto the cortex. *Neuron* **56**, 239–251.
7. Penfield, W., and Boldrey, E. (1937). Somatic motor and sensory representation in the cerebral cortex of man as studied by electrical stimulation. *Brain* **60**, 389–443.
8. Shenoy, K.V., Sahani, M., and Churchland, M.M. (2013). Cortical control of arm movements: a dynamical systems perspective. *Annu. Rev. Neurosci.* **36**, 337–359.
9. Merel, J., Botvinick, M., and Wayne, G. (2019). Hierarchical motor control in mammals and machines. *Nat. Commun.* **10**, 5489.
10. Schwartz, A.B. (2016). Movement: how the brain communicates with the world. *Cell* **164**, 1122–1135.
11. Straka, H., Simmers, J., and Chagnaud, B.P. (2018). A new perspective on predictive motor signaling. *Curr. Biol.* **28**, R232–R243.
12. Ferreira-Pinto, M.J., Ruder, L., Capelli, P., and Arber, S. (2018). Connecting circuits for supraspinal control of locomotion. *Neuron* **100**, 361–374.
13. Grillner, S., and El Manira, A. (2020). Current principles of motor control, with special reference to vertebrate locomotion. *Physiol. Rev.* **100**, 271–320.
14. Kiehn, O., and Dougherty, K. (2013). Locomotion: circuits and physiology. In *Neuroscience in the 21st Century* (Springer), pp. 1209–1236.
15. Clancy, K.B., Orsolic, I., and Mrsic-Flogel, T.D. (2019). Locomotion-dependent remapping of distributed cortical networks. *Nat. Neurosci.* **22**, 778–786.
16. Kaplan, H.S., and Zimmer, M. (2020). Brain-wide representations of ongoing behavior: a universal principle? *Curr. Opin. Neurobiol.* **64**, 60–69.
17. Karadimas, S.K., Satkunendrarajah, K., Laliberte, A.M., Ringuette, D., Weisspapir, I., Li, L., Gosgnach, S., and Fehlings, M.G. (2020). Sensory cortical control of movement. *Nat. Neurosci.* **23**, 75–84.
18. Musall, S., Kaufman, M.T., Juavinett, A.L., Gluf, S., and Churchland, A.K. (2019). Single-trial neural dynamics are dominated by richly varied movements. *Nat. Neurosci.* **22**, 1677–1686.
19. Stringer, C., Pachitariu, M., Steinmetz, N., Reddy, C.B., Carandini, M., and Harris, K.D. (2019). Spontaneous behaviors drive multidimensional, brainwide activity. *Science* **364**, 255.
20. Zatka-Haas, P., Steinmetz, N.A., Carandini, M., and Harris, K.D. (2021). Sensory coding and the causal impact of mouse cortex in a visual decision. *eLife* **10**, e63163.
21. Ahrens, M.B., Li, J.M., Orger, M.B., Robson, D.N., Schier, A.F., Engert, F., and Portugues, R. (2012). Brain-wide neuronal dynamics during motor adaptation in zebrafish. *Nature* **485**, 471–477.
22. Chen, X., Mu, Y., Hu, Y., Kuan, A.T., Nikitchenko, M., Randlett, O., Chen, A.B., Gavornik, J.P., Sompolinsky, H., Engert, F., et al. (2018). Brain-wide organization of neuronal activity and convergent sensorimotor transformations in larval zebrafish. *Neuron* **100**, 876–890.e5.
23. Dunn, T.W., Mu, Y., Narayan, S., Randlett, O., Naumann, E.A., Yang, C.T., Schier, A.F., Freeman, J., Engert, F., and Ahrens, M.B. (2016). Brain-wide mapping of neural activity controlling zebrafish exploratory locomotion. *eLife* **5**, e12741.
24. Hallinen, K.M., Dempsey, R., Scholz, M., Yu, X., Linder, A., Randi, F., Sharma, A.K., Shaevitz, J.W., and Leifer, A.M. (2021). Decoding locomotion from population neural activity in moving *C. elegans*. *eLife* **10**, e66135.
25. Kato, S., Kaplan, H.S., Schrödel, T., Skora, S., Lindsay, T.H., Yemini, E., Lockery, S., and Zimmer, M. (2015). Global brain dynamics embed the motor command sequence of *Caenorhabditis elegans*. *Cell* **163**, 656–669.
26. Kim, D.H., Kim, J., Marques, J.C., Grama, A., Hildebrand, D.G.C., Gu, W., Li, J.M., and Robson, D.N. (2017). Pan-neuronal calcium imaging with cellular resolution in freely swimming zebrafish. *Nat. Methods* **14**, 1107–1114.
27. Mu, Y., Narayan, S., Mensh, B.D., and Ahrens, M.B. (2020). Brain-wide, scale-wide physiology underlying behavioral flexibility in zebrafish. *Curr. Opin. Neurobiol.* **64**, 151–160.
28. Naumann, E.A., Fitzgerald, J.E., Dunn, T.W., Rihel, J., Sompolinsky, H., and Engert, F. (2016). From whole-brain data to functional circuit models: the zebrafish optomotor response. *Cell* **167**, 947–960.e20.
29. Nguyen, J.P., Shipley, F.B., Linderc, A.N., Plummera, G.S., Liua, M., Setrúa, S.U., Shaevitz, J.W., and Leifer, A.M. (2015). Whole-brain calcium imaging with cellular resolution in freely behaving *Caenorhabditis elegans*. *Proc. Natl. Acad. Sci. USA* **113**, E1074–E1081.
30. Susoy, V., Hung, W., Witvliet, D., Whitener, J.E., Wu, M., Park, C.F., Graham, B.J., Zhen, M., Venkatachalam, V., and Samuel, A.D.T. (2021). Natural sensory context drives diverse brain-wide activity during *C. elegans* mating. *Cell* **184**, 5122–5137.e17.
31. Lemon, W.C., Pulver, S.R., Höckendorf, B., McDole, K., Branson, K., Freeman, J., and Keller, P.J. (2015). Whole-central nervous system functional imaging in larval *Drosophila*. *Nat. Commun.* **6**, 7924.
32. Aimon, S., Katsuki, T., Jia, T., Grosenick, L., Broxton, M., Deisseroth, K., Sejnowski, T.J., and Greenspan, R.J. (2019). Fast near-whole-brain imaging in adult *Drosophila* during responses to stimuli and behavior. *PLoS Biol.* **17**, e2006732.
33. Mann, K., Gallen, C.L., and Clandinin, T.R. (2017). Whole-brain calcium imaging reveals an intrinsic functional network in *Drosophila*. *Curr. Biol.* **27**, 2389–2396.e4.
34. Mann, K., Deny, S., Ganguli, S., and Clandinin, T.R. (2021). Coupling of activity, metabolism and behaviour across the *Drosophila* brain. *Nature* **593**, 244–248.
35. Schaffer, E.S., Mishra, N., Whiteway, M.R., Li, W., Vancura, M.B., Freedman, J., Patel, K.B., Voleti, V., Paninski, L., Hillman, E.M.C., et al. (2021). The spatial and temporal structure of neural activity across the fly brain. *Nat. Commun.* **14**, 5572.
36. Tainton-Heap, L.A.L., Kirszenblat, L.C., Notaras, E.T., Grabowska, M.J., Jeans, R., Feng, K., Shaw, P.J., and van Swinderen, B.V. (2021). A paradoxical kind of sleep in *Drosophila melanogaster*. *Curr. Biol.* **31**, 578–590.e6.
37. Harris, D.T., Kallman, B.R., Mullaney, B.C., and Scott, K. (2015). Representations of taste modality in the *drosophila* brain. *Neuron* **86**, 1449–1460.
38. Münch, D., Goldschmidt, D., and Ribeiro, C. (2021). Distinct internal states interact to shape food choice by modulating sensorimotor processing at global and local scales. Preprint at bioRxiv.
39. Pacheco, D.A., Thibierge, S.Y., Pnevmatikakis, E., and Murthy, M. (2021). Auditory activity is diverse and widespread throughout the central brain of *Drosophila*. *Nat. Neurosci.* **24**, 93–104.
40. Cruse, H., Dürr, V., Schilling, M., and Schmitz, J. (2009). Principles of insect locomotion. *Cogn. Syst. Monogr.* **1**, 43–96.
41. Hughes, G.M. (1952). The co-ordination of insect movements. *J. Exp. Biol.* **29**, 267–285.
42. Manton, S.M. (1973). The evolution of Anthropodan locomoting mechanisms part 10: locomoting habits, morphology and evolution of the hexapod classes. *Zool. J. Linn. Soc.* **51**, 203–400.
43. Wilson, D.M. (1966). Insect walking. *Annu. Rev. Entomol.* **11**, 103–122.
44. Berman, G.J., Choi, D.M., Bialek, W., and Shaevitz, J.W. (2014). Mapping the stereotyped behaviour of freely moving fruit flies. *J. R. Soc. Interface* **11**, 20140672.
45. Branson, K., Robie, A.A., Bender, J., Perona, P., and Dickinson, M.H. (2009). High-throughput ethomics in large groups of *Drosophila*. *Nat. Methods* **6**, 451–457.

46. Chun, C., Biswas, T., and Bhandawat, V. (2021). Drosophila uses a tripod gait across all walking speeds, and the geometry of the tripod is important for speed control. *eLife* 10, e65878.
47. DeAngelis, B.D., Zavatone-Veth, J.A., and Clark, D.A. (2019). The manifold structure of limb coordination in walking Drosophila. *eLife* 8, e46409.
48. Kain, J., Stokes, C., Gaudry, Q., Song, X., Foley, J., Wilson, R., and De Bivort, B. (2013). Leg-tracking and automated behavioural classification in Drosophila. *Nat. Commun.* 4, 1910.
49. Katsov, A.Y., Freifeld, L., Horowitz, M., Kuehn, S., and Clandinin, T.R. (2017). Dynamic structure of locomotor behavior in walking fruit flies. *eLife* 6, e26410.
50. Mendes, C.S., Bartos, I., Akay, T., Márka, S., and Mann, R.S. (2013). Quantification of gait parameters in freely walking wild type and sensory deprived *Drosophila melanogaster*. *eLife* 2, e00231.
51. Strauss, R., and Heisenberg, M. (1990). Coordination of legs during straight walking and turning in *Drosophila melanogaster*. *J. Comp. Physiol. A* 167, 403–412.
52. Hsu, C.T., and Bhandawat, V. (2016). Organization of descending neurons in *Drosophila melanogaster*. *Sci. Rep.* 6, 20259.
53. Namiki, S., Dickinson, M.H., Wong, A.M., Korff, W., and Card, G.M. (2018). The functional organization of descending sensory-motor pathways in Drosophila. *eLife* 7, e34272.
54. Aymanns, F., Chen, C.L., and Ramdya, P. (2022). Descending neuron population dynamics during odor-evoked and spontaneous limb-dependent behaviors. *eLife* 11, e81527.
55. Bidaye, S.S., Machacek, C., Wu, Y., and Dickson, B.J. (2014). Neuronal control of Drosophila walking direction. *Science* 344, 97–101.
56. Bidaye, S.S., Latsbury, M., Chang, A.K., Liu, Y., Bockemühl, T., Büschges, A., and Scott, K. (2020). Two brain pathways initiate distinct forward walking programs in Drosophila. *Neuron* 108, 469–485.e8.
57. Cande, J., Namiki, S., Qiu, J., Korff, W., Card, G.M., Shaevitz, J.W., Stern, D.L., and Berman, G.J. (2018). Optogenetic dissection of descending behavioral control in Drosophila. *eLife* 7, e34275.
58. Rayshubskiy, A., Holtz, S.L., D'Alessandro, I., Li, A.A., Vanderbeck, Q.X., Haber, I.S., Gibb, P.W., and Wilson, R.I. (2020). Neural circuit mechanisms for steering control in walking Drosophila. Preprint at bioRxiv.
59. Suver, M.P., Huda, A., Iwasaki, N., Safarik, S., and Dickinson, M.H. (2016). An array of descending visual interneurons encoding self-motion in Drosophila. *J. Neurosci.* 36, 11768–11780.
60. Chiappe, M.E., Seelig, J.D., Reiser, M.B., and Jayaraman, V. (2010). Walking modulates speed sensitivity in Drosophila motion vision. *Curr. Biol.* 20, 1470–1475.
61. Cruz, T.L., Pérez, S.M., and Chiappe, M.E. (2021). Fast tuning of posture control by visual feedback underlies gaze stabilization in walking Drosophila. *Curr. Biol.* 31, 4596–4607.e5.
62. Fujiwara, T., Cruz, T.L., Bohnslav, J.P., and Chiappe, M.E. (2017). A faithful internal representation of walking movements in the Drosophila visual system. *Nat. Neurosci.* 20, 72–81.
63. Kim, A.J., Fitzgerald, J.K., and Maimon, G. (2015). Cellular evidence for efference copy in Drosophila visuomotor processing. *Nat. Neurosci.* 18, 1247–1255.
64. Kim, A.J., Fenk, L.M., Lyu, C., and Maimon, G. (2017). Quantitative predictions orchestrate visual signaling in Drosophila. *Cell* 168, 280–294.e12.
65. Maimon, G., Straw, A.D., and Dickinson, M.H. (2010). Active flight increases the gain of visual motion processing in Drosophila. *Nat. Neurosci.* 13, 393–399.
66. Suver, M.P., Mamiya, A., and Dickinson, M.H. (2012). Octopamine neurons mediate flight-induced modulation of visual processing in Drosophila. *Curr. Biol.* 22, 2294–2302.
67. Chen, C.L., Aymanns, F., Minegishi, R., Matsuda, V.D., V., Talabot, N., Günel, S., Dickson, B.J., and Ramdya, P. (2023). Ascending neurons convey behavioral state to integrative sensory and action selection brain regions. *Nat. Neurosci.* 26, 682–695.
68. Aimon, S., Cheng, K.Y., Gjorgjieva, J., and Grunwald Kadow, I.C.G. (2023). Global change in brain state during spontaneous and forced walk in Drosophila is composed of combined activity patterns of different neuron classes. *eLife* 12, 85202.
69. Cohn, R., Morantte, I., and Ruta, V. (2015). Coordinated and compartmentalized neuromodulation shapes sensory processing in Drosophila. *Cell* 163, 1742–1755.
70. Fisher, Y.E., Lu, J., D'Alessandro, I., and Wilson, R.I. (2019). Sensorimotor experience remaps visual input to a heading-direction network. *Nature* 576, 121–125.
71. Weir, P.T., and Dickinson, M.H. (2015). Functional divisions for visual processing in the central brain of flying Drosophila. *Proc. Natl. Acad. Sci. USA* 112, E5523–E5532.
72. Zolin, A., Cohn, R., Pang, R., Siliciano, A.F., Fairhall, A.L., and Ruta, V. (2021). Context-dependent representations of movement in Drosophila dopaminergic reinforcement pathways. *Nat. Neurosci.* 24, 1555–1566.
73. Strauss, R. (2002). The central complex and the genetic dissection of locomotor behaviour. *Curr. Opin. Neurobiol.* 12, 633–638.
74. Martin, J.P., Guo, P., Mu, L., Harley, C.M., and Ritzmann, R.E. (2015). Central-complex control of movement in the freely walking cockroach. *Curr. Biol.* 25, 2795–2803.
75. Seelig, J.D., and Jayaraman, V. (2015). Neural dynamics for landmark orientation and angular path integration. *Nature* 521, 186–191.
76. Namiki, S., and Kanzaki, R. (2016). The neurobiological basis of orientation in insects: insights from the silkmoth mating dance. *Curr. Opin. Insect Sci.* 15, 16–26.
77. Chen, T.W., Wardill, T.J., Sun, Y., Pulver, S.R., Renninger, S.L., Baohan, A., Schreiter, E.R., Kerr, R.A., Orger, M.B., Jayaraman, V., et al. (2013). Ultrasensitive fluorescent proteins for imaging neuronal activity. *Nature* 499, 295–300.
78. Pfeiffer, B.D., Ngo, T.T.B., Hibbard, K.L., Murphy, C., Jenett, A., Truman, J.W., and Rubin, G.M. (2010). Refinement of tools for targeted gene expression in Drosophila. *Genetics* 186, 735–755.
79. Brezovec, L.E., Berger, A.B., Hao, Y.A., Lin, A., Ahmed, O.M., Pacheco, D.A., Thibierge, S.Y., Murthy, M., and Clandinin, T.R. (2023). BIFROST: a method for registering diverse imaging datasets. Preprint at bioRxiv.
80. Franconville, R., Beron, C., and Jayaraman, V. (2018). Building a functional connectome of the Drosophila central complex. *eLife* 7, e37017.
81. Green, J., Adachi, A., Shah, K.K., Hirokawa, J.D., Magani, P.S., and Maimon, G. (2017). A neural circuit architecture for angular integration in Drosophila. *Nature* 546, 101–106.
82. Green, J., and Maimon, G. (2018). Building a heading signal from anatomically defined neuron types in the Drosophila central complex. *Curr. Opin. Neurobiol.* 52, 156–164.
83. Shiozaki, H.M., Ohta, K., and Kazama, H. (2020). A multi-regional network encoding heading and steering maneuvers in Drosophila. *Neuron* 106, 126–141.e5.
84. Kim, S.S., Rouault, H., Druckmann, S., and Jayaraman, V. (2017). Ring attractor dynamics in the Drosophila central brain. *Science* 356, 849–853.
85. Turner-Evans, D., Wegener, S., Rouault, H., Franconville, R., Wolff, T., Seelig, J.D., Druckmann, S., and Jayaraman, V. (2017). Angular velocity integration in a fly heading circuit. *eLife* 6, e23496.
86. Lu, J., Behbahani, A.H., Hamburg, L., Westeinde, E.A., Dawson, P.M., Lyu, C., Maimon, G., Dickinson, M.H., Druckmann, S., and Wilson, R.I. (2022). Transforming representations of movement from body- to world-centric space. *Nature* 601, 98–104.
87. Lyu, C., Abbott, L.F., and Maimon, G. (2022). Building an allocentric travelling direction signal via vector computation. *Nature* 601, 92–97.
88. Dvořáček, J., and Kodrík, D. (2021). Drosophila reward system - A summary of current knowledge. *Neurosci. Biobehav. Rev.* 123, 301–319.

89. Strother, J.A., Wu, S.T., Rogers, E.M., Eliason, J.L.M., Wong, A.M., Nern, A., and Reiser, M.B. (2017). Behavioral state modulates the ON visual motion pathway of *Drosophila*. *Proc. Natl. Acad. Sci. USA* **115**, E102–E111.
90. Costa, M., Manton, J.D., Ostrovsky, A.D., Prohaska, S., and Jefferis, G.S.X.E. (2016). NBLAST: rapid, sensitive comparison of neuronal structure and construction of neuron family databases. *Neuron* **91**, 293–311.
91. Aso, Y., Sitaraman, D., Ichinose, T., Kaun, K.R., Vogt, K., Belliard-Guérin, G., Plaçais, P.-Y., Robie, A.A., Yamagata, N., Schnaitmann, C., et al. (2014). Mushroom body output neurons encode valence and guide memory-based action selection in *Drosophila*. *eLife* **3**, e04580.
92. Ito, K., Shinomiya, K., Ito, M., Armstrong, J.D., Boyan, G., Hartenstein, V., Harzsch, S., Heisenberg, M., Homberg, U., Jenett, A., et al. (2014). A systematic nomenclature for the insect brain. *Neuron* **81**, 755–765.
93. Bogovic, J.A., Otsuna, H., Heinrich, L., Ito, M., Jeter, J., Meissner, G., Nern, A., Colonell, J., Malkesman, O., Ito, K., et al. (2020). An unbiased template of the *Drosophila* brain and ventral nerve cord. *PLoS One* **15**, e0236495.
94. Avants, B.B., Tustison, N., and Song, G. (2009). Advanced normalization tools (ANTS). *Insight J* **2**, 1–35.
95. Hoffmann, M., Billot, B., Greve, D.N., Iglesias, J.E., Fischl, B., and Dalca, A.V. (2022). SynthMorph: learning contrast-invariant registration without acquired images. *IEEE Trans. Med. Imaging* **41**, 543–558.
96. Moore, R.J.D., Taylor, G.J., Paulk, A.C., Pearson, T., van Swinderen, B.V., and Srinivasan, M.V. (2014). FicTrac: a visual method for tracking spherical motion and generating fictive animal paths. *J. Neurosci. Methods* **225**, 106–119.
97. Avants, B.B., Tustison, N.J., Song, G., Cook, P.A., Klein, A., and Gee, J.C. (2011). A reproducible evaluation of ANTs similarity metric performance in brain image registration. *Neuroimage* **54**, 2033–2044.
98. Scheffer, L.K., Xu, C.S., Januszewski, M., Lu, Z., Takemura, S.Y., Hayworth, K.J., Huang, G.B., Shinomiya, K., Maitlin-Shepard, J., Berg, S., et al. (2020). A connectome and analysis of the adult *Drosophila* central brain. *eLife* **9**, e57443.
99. Dorkenwald, S., McKellar, C.E., Macrina, T., Kemnitz, N., Lee, K., Lu, R., Wu, J., Popovych, S., Mitchell, E., Nehorai, B., et al. (2022). FlyWire: online community for whole-brain connectomics. *Nat. Methods* **19**, 119–128.
100. Yang, H.H., St-Pierre, F., Sun, X., Ding, X., Lin, M.Z., and Clandinin, T.R. (2016). Subcellular imaging of voltage and calcium signals reveals neural processing in vivo. *Cell* **166**, 245–257.
101. Mano, O., Creamer, M.S., Matulis, C.A., Salazar-Gatzimas, E., Chen, J., Zavatone-Veth, J.A., and Clark, D.A. (2019). Using slow frame rate imaging to extract fast receptive fields. *Nat. Commun.* **10**, 4979.
102. Lütcke, H., Gerhard, F., Zenke, F., Gerstner, W., and Helmchen, F. (2013). Inference of neuronal network spike dynamics and topology from calcium imaging data. *Front. Neural Circuits* **7**, 201.
103. Hansen, P.C. (2002). Deconvolution and regularization with Toeplitz matrices. *Numer. Algor.* **29**, 323–378.
104. Bates, A.S., Manton, J.D., Jagannathan, S.R., Costa, M., Schlegel, P., Rohlfing, T., and Jefferis, G.S.X.E. (2020). The natverse, a versatile toolbox for combining and analysing neuroanatomical data. *eLife* **9**, e53305.

## STAR★METHODS

### KEY RESOURCES TABLE

REAGENT or RESOURCE	SOURCE	IDENTIFIER
<b>Deposited data</b>		
Raw and processed neural and behavioral data	This paper	<a href="https://dandiarchive.org/dandiset/000727/0.240106.0043">https://dandiarchive.org/dandiset/000727/0.240106.0043</a>
Neuropil Atlas	Ito et al. <sup>92</sup>	<a href="https://github.com/VirtualFlyBrain/DrosAdultHalfBRAINdomains">https://github.com/VirtualFlyBrain/DrosAdultHalfBRAINdomains</a>
JRC 2018	Bogovic et al. <sup>93</sup>	<a href="https://www.janelia.org/open-science/jrc-2018-brain-templates">https://www.janelia.org/open-science/jrc-2018-brain-templates</a>
<b>Experimental models: Organisms/strains</b>		
<i>Drosophila melanogaster</i> w+/w+; UAS-myr::tdTomato/UAS-GCaMP6f; nSyb-Gal4/+	Mann et al. <sup>33</sup>	N/A
<b>Software and algorithms</b>		
Custom neural and behavioral analysis code	This paper	<a href="https://github.com/lukebrez/brezovec_topography">https://github.com/lukebrez/brezovec_topography</a>
Advanced Normalization Tools (ANTs)	Avants et al. <sup>94</sup>	N/A
Synthmorph	Hoffmann et al. <sup>95</sup>	N/A
FicTrac	Moore et al. <sup>96</sup>	N/A

### RESOURCE AVAILABILITY

#### Lead contact

Further information and requests for resources should be directed to the lead contact, Tom R. Clandinin ([trc@stanford.edu](mailto:trc@stanford.edu)).

#### Materials availability

This study did not generate new unique reagents.

#### Data and code availability

- Microscopy (structural and functional neural recordings) and behavioral data have been deposited at DANDI and are publicly available as of the date of publication. DOIs are listed in the [key resources table](#).
- All original code has been deposited at Github and is publicly available as of the date of publication. DOIs are listed in the [key resources table](#).
- Any additional information required to reanalyze the data reported in this paper is available from the [lead contact](#) upon request.

### EXPERIMENTAL MODEL AND SUBJECT DETAILS

*Drosophila melanogaster* had a genotype of w+/w+;UAS-myr::tdTomato/UAS-GCaMP6f;nSyb-Gal4/+ . Drosophila were housed with molasses medium at 25°C while experiencing a 12/12-h light/dark cycle. Vials contained 10–20 flies of mixed genders, and female flies were imaged at 3–4 days post-eclosion. We chose female flies because they have larger brains and bodies than males making them easier to mount and image. As the animals were group housed with males, they were mated.

### METHOD DETAILS

#### Mounting and dissection

A cold Peltier plate was used to anesthetize flies, using a custom aluminum holder that was thermally coupled to the Peltier plate. After immobilization the fly was positioned into a custom mount built from a custom cut steel shim and 3D-printed plastic dish. UV-curable glue was applied on the face between the eyes, as well as the thorax, to fix the fly to the mount. A dissection saline solution composed of 103 mM NaCl, 3 mM KCl, 5 mM TES, 1 mM NaH<sub>2</sub>PO<sub>4</sub>, 4 mM MgCl<sub>2</sub>, 1.5 mM CaCl<sub>2</sub>, 10 mM trehalose, 10 mM glucose, 7 mM sucrose, and 26 mM NaHCO<sub>3</sub> was added to the dish. A tungsten needle was used to open the posterior head cuticle and expose the whole brain. Fat and trachea were removed with dissection forceps.

### Two-photon imaging

A resonant scanning Bruker Ultima IV system with a piezo drive was used to image the flies. A Leica 20 $\times$  HCX APO 1.0 NA water immersion objective lens was used. A Chameleon Vision II femtosecond laser (Coherent) at 920 nm was used to simultaneously excite GCaMP6f and tdTomato. The emission photons were filtered using a 525/50 nm filter and a 595/50 nm filter respectively, and two GaAsP-type photomultiplier tubes were used to simultaneously collect photons. During the experiment a carbogen-bubbled (95% O<sub>2</sub>, 5% CO<sub>2</sub>) saline solution (same as above) heated to 30°C with an in-line heater was perfused across the brain. A volume rate of 1.8Hz was achieved at a spatial resolution of 2.6 x 2.6 x 5  $\mu$ m (256 voxels x 128 voxels x 49 slices, XYZ). The brain was imaged for 30 min while the animal's behavior was tracked (below) for the functional scan. Scans were bidirectional along the X axis. After this functional data was recorded, an anatomical scan was performed at a resolution of 0.6 x 0.6 x 1  $\mu$ m (1024 voxels x 512 voxels x 241 slices, XYZ). 100 of these volumes were collected to later computationally obtain a high SNR image (below).

### Behavior tracking

During the functional neural recording, the fly's walking behavior was tracked by measuring the rotations of an air-suspended ball (9 mm diameter, LAST-A-FOAM FR4615) on which the fly walked. A Flea FL3-U3-13E4M-C sensor and Edmund Optics 100 mm C Series Fixed Focal Length Lens was used to acquire behavior images at 50 Hz. Optic fibers guided light from an IR LED to illuminate the ball. Fictrac was employed to calculate the animal's walking trajectory (which was computationally extracted based on the pattern of black spots painted onto the ball).<sup>96</sup> Ball velocity was smoothed using a Savitzky-Golay filter of window length 500 ms and a polynomial of order 3. Behavior was recorded for the 30-min imaging period ([Video S1](#)).

### Data preprocessing

ANTs was first used to motion-correct each brain volume.<sup>94,97</sup> To do this, the tdTomato channel was averaged across time for the 30 min recording, followed by warping each tdTomato volume (affine and non-linear) to the temporal average. The warp parameters from each volume were applied to the simultaneously collected GCaMP6f channel. After motion correction, a bleaching correction and high-pass filter was applied to each voxel independently. This was achieved by subtracting a temporally smoothed signal (using a gaussian filter of 2-min sigma, truncated at 1 sigma) from the raw trace. After this high-pass filter, each voxel was independently Z-scored.

### Data alignment

Data was aligned as in BIFROST.<sup>79</sup> Briefly, the 100 collected anatomical volumes of tdTomato were motion corrected and averaged to create the final anatomical scan. Next, each animals' temporally averaged functional scan was aligned to their anatomical scan using an affine transform. The tdTomato channel was used for alignment, which was then applied to the GCaMP6f channel. Each anatomical scan was then aligned to the Functional Drosophila Atlas (FDA), using affine and non-linear transformations, and these were then applied to the GCaMP6f channel.<sup>79</sup> This protocol resulted in the functional data all existing in a common space, the FDA. This space contains anatomical atlas ROIs and connectomes.<sup>92,98,99</sup>

## QUANTIFICATION AND STATISTICAL ANALYSIS

### Agglomerative clustering supervoxel creation

Voxels were aggregated into supervoxels in an effort to boost SNR as well as reduce the number of features for computational tractability. After preprocessing and registering the GCaMP6f neural data (above), flies were temporally concatenated resulting in a single matrix of (x, y, z, t; 256, 128, 49, 30456). Voxels were merged independently for each z-slice using Ward linkage agglomerative clustering, as well as a connectivity constraint, meaning merging was only allowed for spatially neighboring voxels. To determine the optimal number of supervoxels, we searched across a range of supervoxels (1, 100, 500, 1000, 2000, 5000, 10000) and fit a linear model that predicted behavior from the supervoxel neural signals. 2000 supervoxels that minimized prediction error and were therefore used for subsequent analyses.

### Correlation analysis (voxel- and supervoxel- wise)

We started with the full dataset with supervoxels (supervoxel, z, t; 2000, 49, 30456). The Pearson correlation was calculated for each supervoxel and for each of three continuous behaviors: forward velocity, left rotational velocity, and right rotational velocity. Specifically, the correlation was calculated between neural activity and the instantaneous value of the continuous vector describing the velocity component. The threshold for a significant correlation was set as  $p = 0.001$  with a Bonferroni multiple comparison correction (2000 x 49 comparisons), giving a final  $p$  threshold of  $1 \times 10^{-8}$ . Because supervoxels reduce the spatial resolution, we also calculated correlations of the individual voxels (x, y, z, t; 256, 128, 49, 30456). Indeed, we found that in this simple correlation analysis, the individual voxels produced a higher spatial resolution map. However, with so many comparisons, using a Bonferroni correction caused a strong erosion of the map. Therefore, we used the approximate spatial coverage of the supervoxel map with its Bonferroni correction to set a reasonable  $p$ -value threshold for the individual voxel map ( $p = 1 \times 10^{-4}$ ). This resulted in a map with the highest possible spatial resolution, while still using a principled means of setting the significance threshold.

### Unique variance explained modeling

Here, we used behavior to predict neural activity of each supervoxel independently (supervoxel, z, t; 2000, 49, 30456). For each supervoxel, we fit separate models with different combinations of input features: single behavior variables (forward velocity, left rotational velocity, right rotational velocity, and binary walking or not walking), all four behavior variables, or leave-one-out. We calculated the prediction accuracy for each model and for each supervoxel. To calculate the unique contribution of each behavior variable, we subtracted the prediction accuracy of the leave-one-out models from the all-four-variable model. All models were Leave-One-Out cross-validated and regularized with ridge regression. During training we calculated the model error as the negative mean squared error. Final model performance is reported as the square root of the coefficient of determination. Models assume the underlying relationship between the variables is linear, the observations are independent, and the residuals are normally distributed and homoscedastic.

### Cross-correlation analysis

Repeated sampling of behavior and neural activity, combined with precise timestamps of these measurements, allowed a reconstruction of temporal resolution dramatically higher than the imaging rate. Volumes of neural data were collected at 1.8 Hz and behavioral measurements were taken at 50 Hz. Behavioral measurements were triggered using the imaging software, resulting in neural and behavioral timestamps matched to the same clock. The precision of these timestamps was sub-millisecond, including the time at which each individual voxel of neural activity was collected. Next, to compute cross-correlation filters, we took each neural measurement with the associated behavioral data that preceded and followed the neural measurement at the full temporal resolution of 50 Hz. This method allows for temporal super-resolution<sup>100,101</sup>; considering Nyquist sampling, the effective precision of our filters is therefore 25Hz. After this, delays induced by the GCaMP6f sensor were deconvolved (see below).

In detail, cross correlation filters were calculated as follows. Given a matrix of timestamps for each slice of neural data across the dataset (z slice (49 per volume), vol\_num (30,456 volumes in the dataset)), interpolation windows of behavior variables were created, with each window centered on each slice and volume number, with 20 ms steps (corresponding to the 50Hz acquisition) spanning 5 sec before and after each neural measurement (thereby including 500 behavioral measurements). This resulted in a behavior matrix of (z, vol\_num, interp\_window; 49, 30456, 500). This matrix was then weighted by the neural activity for each supervoxel to produce a filter spanning the interpolation window. This resulted in the equivalent of a cross-correlation filter for each supervoxel and for each behavior variable. These filters had a power peak in the frequency spectrum at exactly the volume imaging rate (1.8 Hz), which we subsequently removed with a notch filter. Only the strongest 40% of responding filters were used for analysis, a cutoff selected based on the fact that 40% of the brain displayed statistically significant correlations with behavior (see above correlation analysis).

### GCaMP6f deconvolution

We deconvolved the GCaMP6f indicator kinetics from the cross-correlational filters to get a more accurate measure of the temporal relationship between neural activity and behavior. To achieve this, we used a measured GCaMP6f impulse response take from Tm3 and Mi1, interneurons in the Drosophila visual system.<sup>100</sup> We modeled the impulse kinetics as  $\Delta F/F = (1-e^{-t/4})^*(-e^{-t/8})$ .<sup>102</sup> We expanded this function into a Toeplitz matrix, which allowed us to solve for the deconvolution using least-squares.<sup>103</sup>

### Registration of connectome to functional data

The connectome was registered to our functional neural recordings as done previously.<sup>79</sup> Briefly, the coordinates of the synapses of all neurons in the hemibrain connectome were fetched using neuropil, and transformed into the space of JRC2018F using the fly-brains Python package.<sup>104</sup> This was followed by registering JRC2018F into our Functional Drosophila Atlas using BIFROST, and applying the transforms to the synapses.<sup>79</sup>

### Parcellation of functional data for comparison to connectome

We wished to parcellate the functional data on a spatial scale that did not exceed the spatial accuracy of the connectome to functional data registration. Previous work estimated this accuracy to be approximately 5um. Additionally, we wished to agglomerate across z-slices to form 3-dimensional clusters. As before, we used agglomerative clustering with Ward linkage and a connectivity constraint on the full neural recording time series. Because we were fitting the entire volume of neural data at once (i.e. across z-slices), we used neural data from only one representative individual fly to facilitate the computation. Before clustering, we masked all voxels that did not contain any synapses in the hemibrain connectome. We selected a median cluster size of 1,000um<sup>3</sup>, or approximately 10μm in diameter, which was achieved with 5,000 clusters.

### Connectivity of functional regions

For each of the 5,000 clusters, we calculated the correlation of the cluster-averaged neural activity from the entire dataset (9 flies) to behavior (forward velocity and ipsilateral turning velocity). We then binarized these clusters as either containing information about behavior, or not (separately for forward and turning), by setting three Pearson's R correlation thresholds of 0.1, 0.15, and 0.2. This gave us three increasingly strict binary maps of the spatial distribution of the velocity signals. We then calculated the connectivity of each velocity map at each correlation threshold as defined by the hemibrain connectome. To do this, we calculated an adjacency matrix for the 5,000 clusters. This matrix describes how synaptically connected each cluster is to every other cluster. Here we defined connectivity as the number of pre-synapses in a given cluster, multiplied by the number of post-synapses in a second given cluster, if

those synapses belonged to the same neuron. For example, if a particular neuron has 10 pre-synapses in cluster A, and 5 post-synapses in cluster B, the connectivity score is 50. This score was summed across all neurons and divided by the volume of cluster A plus the volume of cluster B to give a normalized connectivity score. This value forms an entry in the adjacency matrix. To calculate the connectivity between clusters that contained a particular behavior signal, we considered each possible pair of clusters that exceeded the correlation threshold. We split these pairs into bins based on the Euclidian distance between the centroids of each cluster, because we expected the distance to influence the connectivity (closer clusters will be more synaptically connected). For each distance bin, for each behavior, and for each behavior correlation threshold, we calculated the average connectivity between pairs of clusters. Importantly, we needed to calculate the null distribution of how connected any two randomly selected clusters were in order to show that the functionally defined regions were more connected than expected. Next, considering all clusters, for each distance bin we selected a number of cluster pairs that equaled the number of pairs for the corresponding behavior variable and corresponding distance bin, and calculated their connectivity. We repeated this sampling with replacement (bootstrap) 1,000 times to form a null distribution of expected connectivity.

#### Identification of neural networks underlying functional signals

A schematic of the workflow of this method is in [Figure S6D](#), and the resulting graphs are in [Figure S7](#). For each neuron in the hemibrain connectome, we calculated the fraction of its synapses that were contained within a given behavior mask. Behavior masks were created by binarizing the unique variance explained maps from [Figure 5](#) based on a threshold value that best captured the shape of the mask while excluding high spatial frequency noise. We then swept across a range of thresholds of “fraction of synapses in mask”, taking the pool of neurons that exceeded each increasingly strict threshold. For each of these pools, we then swept across another threshold based on connectivity, i.e., we assigned each neuron a connectivity score based on how well it was connected to all the other neurons in the same pool; then for each connectivity threshold we only took the neurons that were above threshold. Connectivity was defined as the average number of synapses with other neurons in the pool. These two steps represent a 2D grid search of the two variables. Each pair of thresholds corresponds to a network of neurons that has a location within the 2D space defined by % synapses and connectivity. Within this 2D space, we drew two sets of isocontours. One set comprised the Sørensen-Dice scores of the network (i.e., not the Sørensen-Dice scores of individual neurons, but rather the Sørensen-Dice score of the collective network), and another set for the number of neurons in the network. Each set of isocontours were monotonic and contained inflection points, allowing us to select a single contour at the inflection point. The selected isocontours for the number of neurons and the network Sørensen-Dice score were used to define a boundary for neural networks that should be considered most likely to underly the particular behavior map. We then pooled the networks that were within the boundary. Finally, we repeated this entire process, but used a different initialization metric, namely the neuron’s Sørensen-Dice score. This resulted in two networks, which we then intersected to select only those neurons that were identified from both approaches. As a result, selected neurons have a relatively large fraction of their volume (via Sørensen-Dice initialization), as well as a relatively large fraction of their synapses (via the fraction of synapses initialization) within the behavior mask.

#### Comparing identified neurons with next most similar candidates

Related to [Figures S7E–S7H](#). We wished to assess whether our identified neural candidates were similar in morphology and connectivity to other neurons that were not identified by our approach. That is, if we replaced a given identified neuron with the next most morphologically similar neuron in the connectome, does this alternate neuron display comparable overlap with our behavioral map, and comparable connectivity to the original network. To quantify this, we took advantage of each neuron’s NBLAST score, which quantifies morphological similarity between any pair of neurons.<sup>90</sup> We started with a matrix that contained the pairwise NBLAST score of every neuron in the hemibrain connectome. We then did the following for each candidate neuron identified in the turning network. First, we replaced each candidate with the neuron to which it had the greatest pairwise NBLAST score. Second, we calculated the Sørensen-Dice score between this new neuron and the turning behavior mask (as above), and subtracted the original neuron’s Dice score, giving a difference in Dice scores. Third, we calculated the number of synapses this new neuron had with all other neurons in the original turning network and subtracted the original neuron’s number of synapses with the network, giving a difference in synapse count. Finally, we considered the rank of the new neuron. That is, when selecting the next most morphologically similar candidate by NBLAST score, we excluded neurons that were already included independently within the turning network. In these cases, we iteratively moved down the NBLAST score ranking list until we identified a unique alternative neuron to test.